Fast Photodiode Diagnostic on Alcator C-Mod Tokamak to Study the Plasma Edge/SOL Structure

by

Bálint Vető

S.B. Natural Sciences (2002)
University College Utrecht

Submitted to the Department of Nuclear Science and Engineering
in partial fulfillment of the requirements for the degree of

Master of Science

at the

MASSACHUSETTS INSTITUTE OF TECHNOLOGY

September 2005

Author .....
Department of Nuclear Science and Engineering
July 25, 2005

Certified by ..... 8/18/2005 .....
Dr. James Terry
Research Scientist, Plasma Science and Fusion Center
Thesis Supervisor

Certified by ..... 18 Aug 05 .....
Professor Ian Hutchinson
Head, Department of Nuclear Science and Engineering
Thesis Reader

Accepted by .....
Professor Jeffery A. Coderre
Chairman, Department Committee on Graduate Students

Fast Photodiode Diagnostic on Alcator C-Mod Tokamak to Study the Plasma Edge/SOL Structure

by

Bálint Vető

Submitted to the Department of Nuclear Science and Engineering
on July 25, 2005, in partial fulfillment of the
requirements for the degree of
Master of Science

Abstract

The tokamak is so far the most promising magnetic confinement configuration to control fusion scale plasmas and to be a large scale source of electricity in the future. Built in the shape of a torus of major and minor radius R and r respectively, the charged particles are confined by the superposition of a toroidal and a poloidal magnetic field. In order to study the transport processes that lead to the removal of energetic particles from the hot plasma, two tangentially viewing optical diagnostics have been installed to look at the plasma edge region ($0.9 < \frac{x}{r} < 1.1$) of the Alcator C-Mod diverted tokamak. The toroidally looking views are coupled to fast photodiode amplifier circuits that record the D_α brightness at a rate of 1 MHz. Two plasma-directed gas puffs are employed at the inboard and outboard plasma edges to enhance the emission at the desired toroidal locations. The absolutely calibrated views yield the required data for building radial and poloidal profiles of the intrinsic D_α plasma brightness. The Abel inverted radial D_α emissivity profile typically peaks at 30 W/m^3/ster at 1 cm outside the separatrix ($\frac{x}{r} \approx 1.05$) and drops on both sides of the separatrix. For the first time, the poloidal measurements of the plasma edge brightness with and without the D_2 neutral gas puff yielded an estimate for the vertical extent of the neutral gas puff. The steady state inboard and outboard D_α brightness profiles are also compared during two consecutive periods of L and H mode operation. The time lagged cross correlation calculated for neighboring views revealed quickly propagating local brightness maxima (blobs). The phase velocity of these systematically moving brightness perturbations ranges from -1 to 1 km/s inside the separatrix and becomes uniform outside the separatrix at 0.5 km/s where the positive velocity indicates radially outward motion. Downward propagating perturbations are also observed in the outboard SOL.

Thesis Supervisor: Dr. James Terry
Title: Research Scientist, Plasma Science and Fusion Center

Thesis Reader: Professor Ian Hutchinson
Title: Head, Department of Nuclear Science and Engineering

Abstract

Le tokamak est de loin la configuration la plus prometeuse pour confiner par champs magnétique des plasmas dediés à la fusion et constituer ainsi une source d'énergie à grande echelle pour le futur. Les particules chargées sont confinées dans un tore de grand et petit rayons R and r par la superposition de champs toroidal et poloidal. Afin de mieux comprendre les processus de transport qui conduisent à une perte d'energie pour le plasma chaud, un détecteur en forme de croix a été installé sur le tokamak Alcator C-Mod pour observer le bord du plasma ($0.9 < \frac{x}{r} < 1.1$). Chaque vue toroidale est couplé avec un circuit d'amplification des photodiodes rapides qui enregistre des fluctuations de brillance du plasma à la longeur d'onde D_α avec une fréquence de 1 MHz. Le dispositif utilise une injection de gaz neutre dirigée radialement vers l'intérieur afin d'augmenter l'emission à un angle toroidal predeterminé. Les vues sont calibrées de manière absolue et permettent de construire le profil de la brillance radial et poloidal. Le profil radial culmine juste à l'extérieur de la séparatrix à une valeur de 30 W/m^3/ster et diminue vers zéro des deux côtés. La différence entre les profils poloidals avant et après l'injection de gaz neutre estime la taille verticale de l'injection de gaz à 5 cm. La correlation retardée est calculée pour les vues voisines et permet d'observer la propagation de structures à caractère d'ondes appelées blobs. La vitesse de phase de ces blobs est de -1 à 1 km/s à l'intérieur de la séparatrix et devient uniforme à l'extérieur avec une valeur moyenne à 0.5 km/s, les vitesses positives indiquant un mouvement vers l'extérieur.

Acknowledgments

This thesis would have not been possible without support from the many individuals and organizations that shaped my professional and personal life since the day I entered M.I.T. Therefore, I would first like to thank Prof. Michael Driscoll, who was my mentor during the summer of 1998 at the Research Science Institute, organized by the Center for Excellence in Education. His introduction to academic research and encouragement later to pursue the field of nuclear engineering started a series of unexpected and highly rewarding events which, I hope, is still continuing.

Second, I would like to thank the Department of Nuclear Engineering at M.I.T, for giving me the opportunity and the academic framework for the completion of this graduate program and this master's thesis. Just to name a few of my favorites, it was a privilege to attend courses by Prof. Kim Molvig (Introduction to Plasma Physics), Prof. Mujid Kazimi (Engineering Principles), Prof. Sidney Yip (Neutron Interactions), Prof. Ron Parker (Fusion Energy), Prof. Ian Hutchinson (Plasma Diagnostics), Prof. John Deutch (Application of Technology).

I need to say thank you to Prof. Ian Hutchinson also for serving as my thesis reader and as the head of the Alcator group at the Plasma Science and Fusion Center, for offering me the R.A. appointment back in the fall of 2002. I thank Dr. Earl Marmar current leader of the Alcator group for securing the flow of R.A. support.[1]

Now, I want to express my gratitude to those who the spent the most time with me, my fellow graduate students at the department. My office mates Noah Smick, Liang Lin, Eric Edlund, Brock Böse, Arturo Dominguez, Alex Parisot, Brian Youngblood, Paul Antohi and Alex Graf, you were always there to give moral support whether commiserating over over-due homework or going to Anna's for a juicy super steak. Special thanks to Noah for putting up with my loud phone conversations in languages strange to you, to Liang for always discussing the meaning of life, to Eric for the squash games, to Alex for the French revision of the abstract, to Brock for the guy talk and to Arturo for the rum. Let us not forget the invaluable scientific insight and

[1]Supported in part by the U.S. Department of Energy Contract No. DE-FC02-99ER54512.

the simulating technical discussion that you shared with me over the years. I truly believe that I have learned just as much from you as I have from my professors.

I also remember the kindness of the staff the Alcator C-Mod group, without any intention of completeness, I thank Corinne Fogg, Valerie Censabella, Donald Nelson, Bruce Lipschultz, Brian Labombard, Bob Granetz, Nils Basse, Miklós Porkoláb, for their support. Special thanks for Manny for keeping my office and the facilities clean with such discipline day after day, week after week.

I give thanks to other friends and roommates I have had in the past years during graduate school for getting to know you. Yann LeTallec, Scott Rhodes, Mike Demkowitz, Péter Csatorday, Dávid Végh, thank you for sharing your meals with me, involving me in your elevating scientific discussions and social gatherings. Memorable in my heart is Wellesley woman Yin Zhou for the joyful moments we shared. I will also not forget those cookies freshly delivered to the lab. Thank you.

My grateful words and love go to my parents, Kati and Balázs and my sister Sári. Your never ending support and attention bridging the ocean often reached me in the form of e-mails, phone calls and occasional visits. Your encouraging words during the completion of this thesis were well received. At milestones of my life such as this one, I think of you, I hope I make you proud.

Lastly, as all of you know, my research in the Alcator C-Mod research group and my thesis would have not been possible without Dr. James Terry. Jim, I am forever indebted for your professional guidance, assistance and leadership. In addition to the tricks of the trade I have learned from you by closely working with you, you have amazed me with your infinite patience and humility. I greatly appreciate all your time and wisdom, I feel very lucky to have had you as my advisor.

Contents

List of Figures

List of Tables

Chapter 1

Fusion energy

The formation of elementary particles, followed by the formation of stars and planets, the nuclear synthesis of the elements via fusion has been a prerequisite for human life. Nothing shows this more than the fact that all other forms of energy production are using earlier products of fusion reactions.

The radiation from our Sun, weather enabling plant growth via photosynthesis or producing electricity in photo-voltaic panels, is the by-product of various fusion reactions occurring inside the gravitationally confined hot plasma. The radioactive isotopes of uranium and other fission fuels are also the results of multi-step fusion reactions formed under extreme physical conditions in stellar processes.

The energy gained by burning fossil fuels for example, is the electric potential energy of interatomic bonds. The carbon, oxygen, nitrogen, and other elements constituting the fossil fuels, however, were also formed inside stars, most of them in our Sun and it was the solar energy that enabled the synthesis of fossil fuels mostly from water and carbon-dioxide. Yet, this common and ancient source of energy is very challenging for mankind to exploit peacefully and use as a source of electricity.

There is plenty of fusion fuel left in our universe as the lower mass number elements are still the most abundant. Figure 1-1 shows the chemical composition of the solar system [17]. The abundance of elements on Earth is naturally very different from the astrophysical abundances, but due to the massive amounts of water in the oceans and in the atmosphere, hydrogen as a fusion fuel is still essentially unlimited when

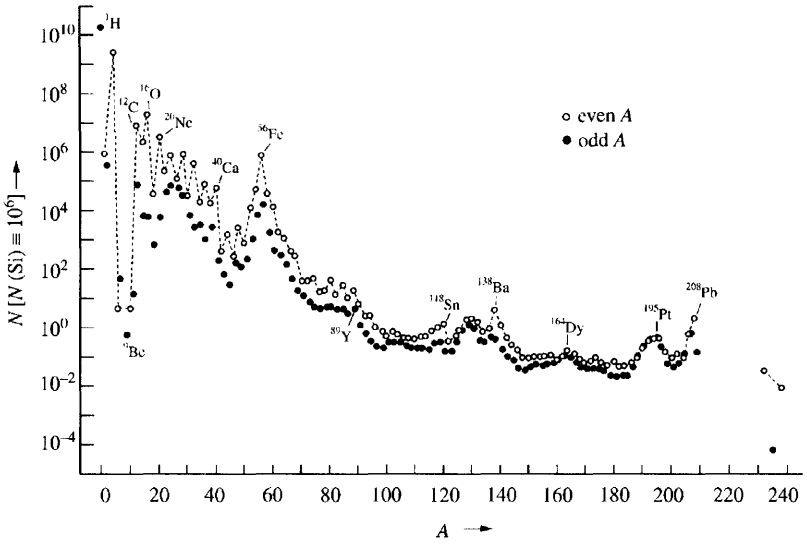

Figure 1-1: Solar system abundances by mass number. Lighter elements evolve toward heavier elements by nuclear fusion reactions. Hydrogen is still the most abundant element of all.[17]

compared to the availability of fission fuels such as the radioactive isotopes of uranium.

Because most fusion reactions require high temperatures and pressures, laboratory plasma physics is mostly focused on the fusion of very light elements consisting only of a few protons and neutrons. Fusion reactions with magnetic confinement interest today are the following:

$$D + D \rightarrow {}^{3}He + n + 3.27 \text{ MeV} \tag{1.1}$$

$$D + D \rightarrow T + p + 4.03 \text{ MeV} \tag{1.2}$$

$$D + T \rightarrow {}^{4}He + n + 17.6 \text{ MeV} \tag{1.3}$$

$$D + {}^{3}He \rightarrow {}^{4}He + p + 18.3 \text{ MeV} \tag{1.4}$$

The resulting net kinetic energy in the above fusion reactions is always split between the two fusion products. Depending on the design of the fusion reactor, the charged particles can be confined using a magnetic field so that the fusion products will transfer their kinetic energies to the plasma. The fusion energy can be removed

from the vessel via the energetic neutrons that are slowed down in a blanket serving as a moderator. As the confinement of the edge plasma is not perfect in current designs, the escaping energetic particles collide into the plasma facing materials, which, in turn, heat up. A specially designed part of the plasma wall, to which a high particle flux is directed, is called the divertor. The divertor of a reactor will be cooled actively because the maximum divertor temperatures are limited by the physical properties of the divertor material. The removed high temperature heat then can be utilized with high efficiencies.

1.1 Tokamaks

The word *Tokamak* comes from the concatenations of Russian words meaning, "Toroidal Chamber Machine". Historically, the tokamak was developed from a cylindrical plasma by simply bending it into a torus. The first cylindrical plasma discharge devices were called z-pinches and θ-pinches. In a z-pinch, it is the plasma discharge that carries the current in the longitudinal (z) direction. The magnetic field is only due to the plasma current, so when the plasma current vanishes there is no background magnetic field. In a θ-pinch an externally applied magnetic field induces a large diamagnetic current.

The performance of cylindrical confinement devices were always limited by their end losses. The confinement time can be increased by increasing the length of the discharge tube, but that greatly increases the cost of the hardware. The end loss problems were overcome when the cylindrical magnetic field configuration was transformed into the shape of a torus.

The typical tokamak has the field and induction components of both a z-pinch and a θ-pinch. The primary, toroidal, magnetic field is produced by external poloidal coils, and the inductively created plasma current creates the poloidal magnetic field. The resulting net field line on the surface of the torus will be of a helical shape, with the magnetic field lines spiraling around the surface of the torus. In addition to the toroidal and poloidal magnetic field, position control coils are used to control the

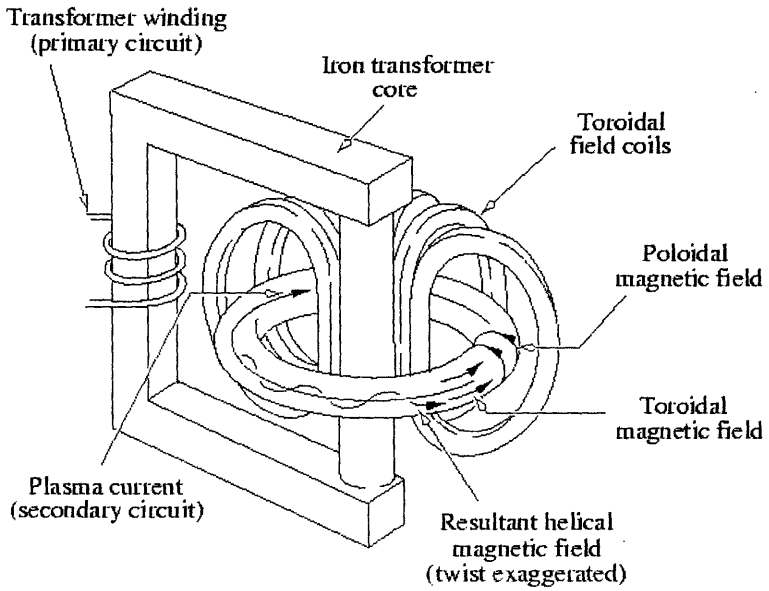

Figure 1-2: Basic structure of a tokamak

position and the shape of the confined plasma. They also play a basic role in the three dimensional toroidal stability.

1.2 Ignition and Operation Requirements

In 1957, J. D. Lawson [15] derived a simplified, but powerful, relationship involving the plasma ion density (n_i), ion temperature (T_i) and confinement time (τ_E). The confinement time is defined as the time required for the plasma to lose its internal energy without any addition of energy. The longer the confinement time, the better the plasma confinement is and the less auxiliary heating is required for creating a burning plasma. For a D-T plasma, the requirement for ignition can be expressed as,

$$nT\tau_E > 5 \times 10^{21} m^{-3}\text{keVs}. \tag{1.5}$$

The cross section for the D-T fusion reaction has a strong temperature dependence and has a maximum around 25 keV.

There have been many theories put forward to describe confinement in fusion plasmas. The energy confinement time τ_E is found to be much shorter than the neo-

classical value. Thus, the relationships used to predict the performance of tokamaks are largely empirical. Magnetically confined fusion experiments can be categorized by the method of heating. Plasmas can be heated ohmically, by radio frequency waves and by the injection of energetic neutral beams. Ordinary, ohmically heated plasmas operate in low confinement mode or L-mode by definition. L-mode confinement does not have a steep edge gradient in plasma pressure, because there is no edge transport barrier (ETB) present. Radio frequency heating and neutral beam injection as well as some ohmically heated plasmas, sometimes produce a better regime of confinement, also referred to as the high confinement mode or an H-mode. To quantify the improvement in confinement time the H factor is introduced, defined as

$$H = \frac{\tau_E}{\tau_E^L}. \tag{1.6}$$

The H-mode confinement is a result of a transport barrier at the edge of the plasma, just inside the last closed flux surface or LCFS. This barrier causes increased pressure and temperature gradients at the plasma edge. In typical recent plasma experiments on C-Mod, plasma discharges with a higher level of confinement have $H \approx 2$. Other improved confinement modes on the TFTR tokamak, made possible by the injection of neutral beams, enabled $H = 3.8$ with low recycling of particles and peaked density profiles.

The plasma outside the last closed magnetic flux surface (LCMFS) of magnetic confinement devices is called the scrape-off layer or SOL. In other words, the SOL is made up of particles that already diffused out of the last closed magnetic flux surface but have not hit the wall yet. The SOL is characterized by the electron temperature (T_e), electron density (n_e) and the typical parallel to $\bar{B}$ distance that a particle has to travel before colliding into a material surface. The average time spent in the SOL, $\tau_{SOL} = L/c_s$ is the ratio of the average trajectory length and the plasma sound speed given by

$$c_s \approx \sqrt{\frac{k(T_e + T_i)}{m_i}}. \tag{1.7}$$

T_e	20	eV
n_e	3×10^{19}	m^{-3}
L	8	m
τ_{SOL}	0.2	ms

Table 1.1: Typical SOL conditions of Alcator C-Mod. Adapted from Stangeby [18]

1.3 Development of plasma diagnostics

Historically, many different methods for diagnosing the plasma discharge have been developed and used. The first instruments were coils that measured the magnetic fields at different radial locations and helped to reconstruct the magnetic topology and current profile of the discharge. These methods are crucial in setting up stable plasmas and to investigate MHD instabilities. Diagnostics are crucial in determining the energy confinement time, the energy loss from the plasma, and estimating transport coefficients. When auxiliary heating is used, new diagnostics are required to measure how efficient the supplemental heating is, and how efficiently was the external energy coupled to the plasma. The diagnostic employed in the research described here is among the group of diagnostics that measures fluctuations and attempts to understand their impact on plasma transport.

1.3.1 Plasma edge as a boundary condition

Turbulent convective transport plays an important role in the energy loss from plasmas. Not all losses can be accounted for by the classical and neoclassical transport processes. The term anomalous transport was introduced to refer to all other types of transport mechanisms not explained by the classical and neoclassical transport.

Diagnosing the plasma edge, or in other words the region near the separatrix where $0.9 < \frac{x}{r} < 1.1$ is an attractive field of research for two reasons. Firstly, the energy and particle transport occurring at the plasma edge serves as a boundary condition for the entire transport picture of the plasma as shown dramatically in the H-mode phenomenon. Secondly, while recent, near fusion scale plasmas have central

temperatures of the order of 10 keV, much too high for typical bound to bound atomic processes, the partially ionized plasma edge region with temperatures of the order of 10 eV, are ideal sources for spectroscopic measurements in the visible spectral region. The edge plasma is also more easily accessible by mechanical probes.

1.3.2 Fluctuations in the plasma edge

Fluctuations in the edge plasma refer to the variations of the plasma density, temperature, electric or magnetic field. Fluctuations, without further conditions, do not result in net transport of particles or energy. There are however situations, when a constellation of conditions on the direction and the phase of oscillation will result in net transport. M. Endler et al. [7] in 1995 provided an excellent review and model for electrostatic fluctuations in the scrape off layer of the ASDEX tokamak.

The purely electrostatic fluctuations, without fluctuations in the magnetic field, result in a particle flux of,

$$\Gamma_r = \tilde{n}\frac{\tilde{E}_\theta}{B_\phi}. \tag{1.8}$$

This flux can be averaged over time to get

$$\bar{\Gamma}_r = \frac{1}{B_\phi}\langle \tilde{n}\tilde{E}_\theta \rangle. \tag{1.9}$$

It follows from Eq. 1.9 that if the density is non fluctuating then there is no transport coupled to the oscillation. The quantity $\frac{\tilde{E}_\theta}{B_\phi}$ is also referred to as the radial drift velocity, $\tilde{v}_r$. In other words, the poloidal component of the electric field and the toroidal magnetic field are the drivers of this cross-field flux. When $\tilde{n}$ and $\tilde{v}_r$ are positive at the same time, the resulting flux is radially outward.

Neoclassical transport can not explain the high values of χ measured on TFTR by Zarnstoff [6]. The discrepancy between the neoclassical prediction and experiment increases near the plasma edge. At a minor radius of 0.6 m, there are two orders of magnitude of difference as shown in Fig. 1-3.

Myra et al. [16] argue that convective, bursty processes in the scrape off layer are

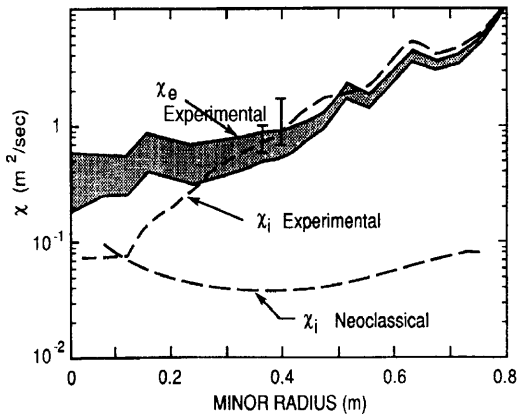

Figure 1-3: Experimental measurement of χ by M. C. Zarnstorff [6]

relevant to the density limit. Based on the BOUT 3D turbulence code, filament like structures are produced from the correlation of monopole density and dipole vorticity structures that convect radially outward.

1.3.3 D_α emission

The optical diagnostic described in this work measures neither $\tilde{n}$ nor $\tilde{E}_\theta$ directly. Rather it measures fluctuations in the D_α emission that result from fluctuations in the local electron density and/or temperature. The emissivity, ϵ is a result of electron impact excitation and can be compactly expressed as

$$\epsilon \propto n_0 n_e Q(T_e, n_e), \tag{1.10}$$

where Q is the excitation rate coefficient. Since in these experiments we reasonably assume that n_0 is not fluctuating at the frequencies of interest (see Zweben [11], Terry [4]), any fluctuation in ϵ is a result of fluctuations in n_e and/or T_e. Modeling of gas puff imaging by Stotler [3] and Zweben [11] has shown that the D_α emissivity can be parameterized for the expected experimental conditions as

$$\epsilon \propto n_e^\alpha T_e^\beta, \tag{1.11}$$

where $0.5 < \alpha < 0.8$ and $0.3 < \beta < 1.4$.

Thus, it is important to keep in mind that while the emission fluctuations measured and discussed here are a result of fluctuations in the local background electron density and temperature, they do not correspond to either of these quantities directly nor are they capable of yielding a particle flux as discussed above.

Chapter 2

Methods

2.1 Alcator C-Mod overview

The Alcator C-Mod (C-Mod) tokamak is located at MIT, Cambridge, MA and was first operated in 1993. It is the successor of Alcator-A and Alcator-C tokamaks. Alcator C-Mod was designed as a high magnetic field, compact tokamak, with a resulting high $\frac{B_\phi}{R}$. The toroidal field can be as high as 8T, with plasma currents of 0.4 to 2.0 MA. The cross section of the plasma has a D-shape with a major radius of 0.68 m and an average minor radius of 0.22 m. These characteristics make it possible for the C-Mod experiment to tap into a new subset of the parameter space and to augment empirical scaling laws at these unique parameters.

Parameter	Symbol	Value
Major radius	R	0.67 m
Minor radius	r	0.22 m
Toroidal magnetic field	B_T	$\leq$ 8 T
Plasma current	I_p	$\leq$ 2.0 MA
Electron density	n_e	$\leq 1.1 \times 10^{21}\ m^{-3}$
Electron temperature	T_e	$\leq$ 6 keV
ICRF heating	P_{RF}	$\leq$ 5 MW
Elongation	κ	0.95 - 1.85

Table 2.1: Alcator C-Mod parameters as of 2005 January. A lower hybrid current drive auxiliary heating system has just been installed that is hoped to deposit additional energy to the discharge and yield more control over the radial current profile.

Most of the plasma facing tiles are made of molybdenum, and are designed to withstand high heat fluxes during operation. C-Mod has a closed divertor, in which three modes of divertor operation have been observed. These regimes of operation are the sheath limited, conduction limited and the detached divertor plasma, for which there exists a pressure drop along the magnetic field.

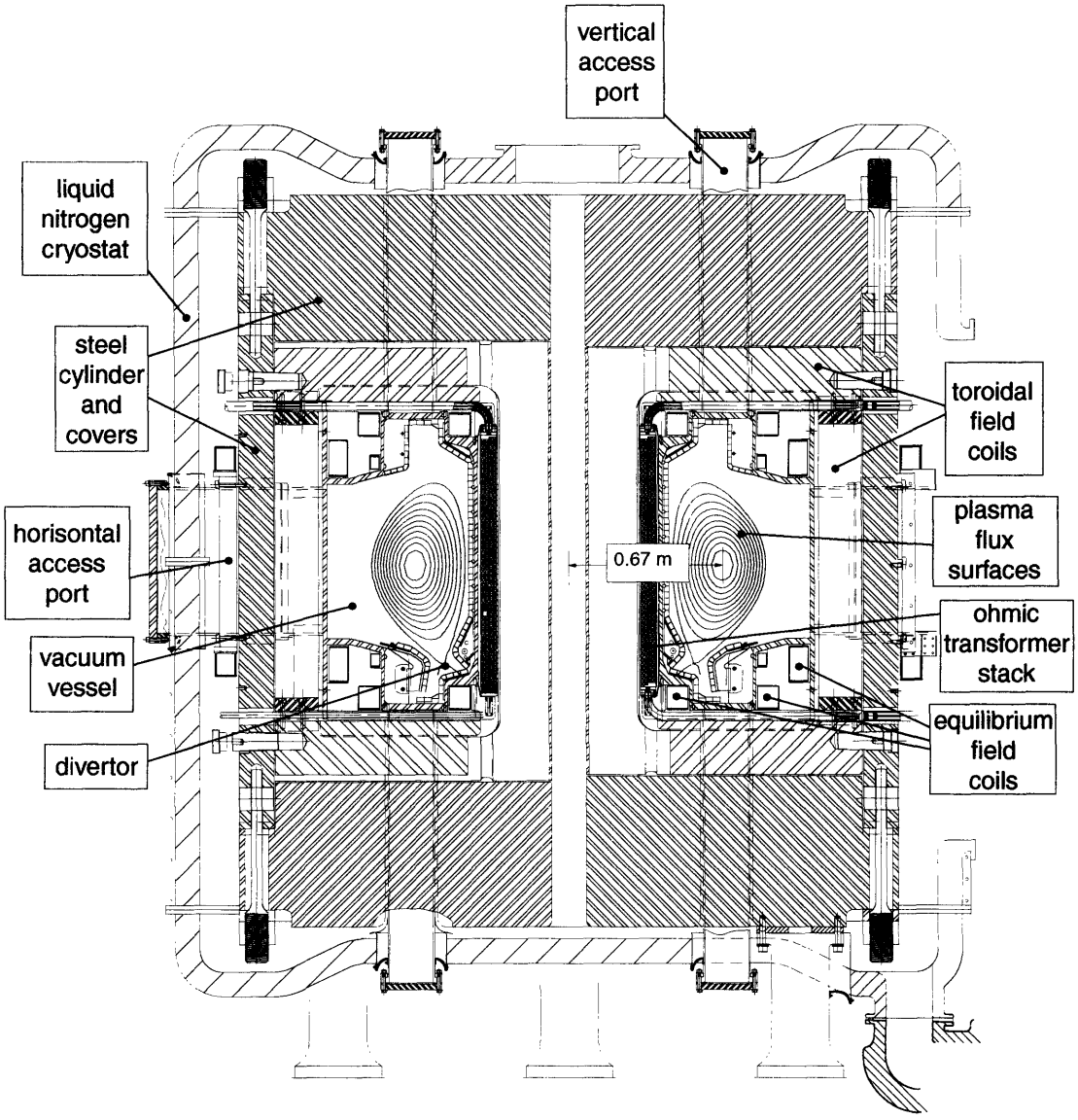

Figure 2-1: The major components of the Alcator C-Mod tokamak

Fig. 2-1 shows a cross sectional view of the Alcator C-Mod tokamak. The concentric red lines show magnetic and pressure iso-surfaces. The pressure and temperature

gradually increase from the outside to the inside reaching a maximum electron temperature of 6 kev in the middle. Not shown on the figure, are the numerous diagnostic instruments that access the vacuum chamber via the horizontal and vertical access ports.

2.2 Fast photodiode diagnostic overview

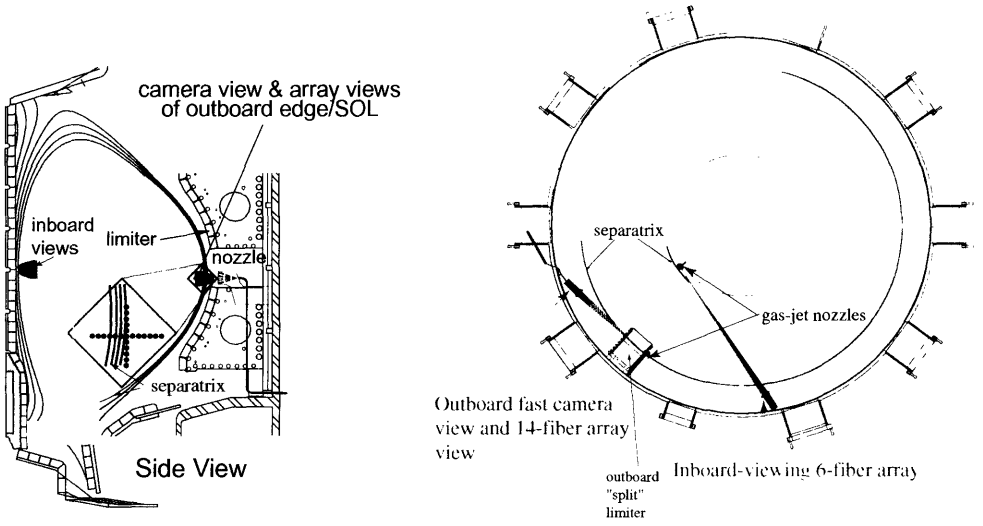

(a) (b)

Figure 2-2: (a) Side view of the GPI and the fast photodiode diagnostic. (b) Top view of the GPI and the fast photodiode diagnostic. Note that the 14-fiber array has been upgraded to the current 40-fiber radial and poloidal viewing array.

The fast photodiode diagnostic on Alcator C-Mod was designed to measure plasma edge fluctuations as well as the steady state radial profiles of D_α emissions. The diagnostic consists of several components. To localize the measurement toroidally and to enhance the intensity of D_α emissions near the scrape-off layer (SOL), a neutral gas cloud is puffed locally into the plasma edge. The puffed gas penetrates the plasma, undergoes ionization and enhances the bound-bound emissions already present in the region. Fig. 2-2 (a) shows a poloidal cross section of the vacuum chamber. The focal spots of both inboard-viewing and outboard-viewing telescopes are shown schematically, with the magnified outboard array to show further details.

Both views span the separatrix and are located near the mid-plane of the torus. Plot (b) shows a from above view, on which the tangential views of the telescopes are visible. The location of the gas jet nozzles coincides with the region where the telescope views are focused.

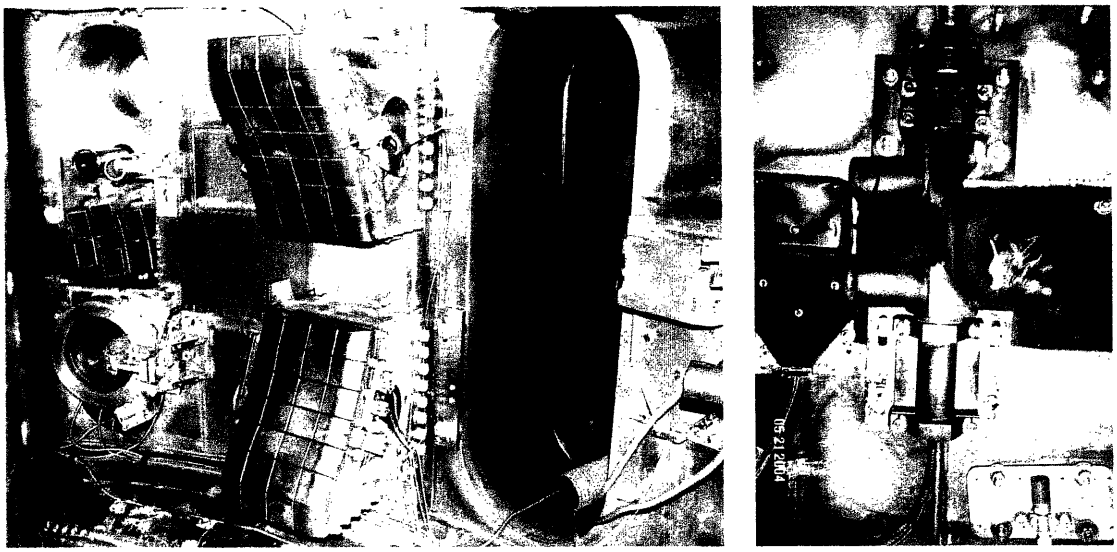

Figure 2-3: In-vessel view of the fast photodiode outboard-viewing telescope and the outboard gas puff nozzle located in the left photo at the left at the bottom of the split on the A-B limiter.

Fig. 2-3 is the in-vessel view of a section of the outboard wall to which the viewing telescope is mounted. On the right there are two viewing telescope ends. Both telescopes focus near the mid-plane. The telescope on the lower right carries optical signal to the fast photodiodes, the one above is used for the ultra-fast camera sister diagnostic. The nozzle, located between the two array of tiles on the left, was designed to produce a toroidally localized, shock-wave free gas cloud.

2.3 System integration of the fast photodiode diagnostic

The optical signals from the views inside vacuum chamber are carried by optical fibers. The optical fibers leave the vessel via a bottom vertical port where a special

vacuum feed-through flange is installed. The fibers end at a breakout box, where another set of individually jacketed optical fibers (transfer fibers on 2-4) is used to provide the input signal to the photodiode amplifier boxes. A good deal of care is needed to keep record of the exact configuration of the fiber connections. Not only do different views have different intensities, but the different fibers differ in their relative levels of signal transmission as there are losses associated with the signal transfer.

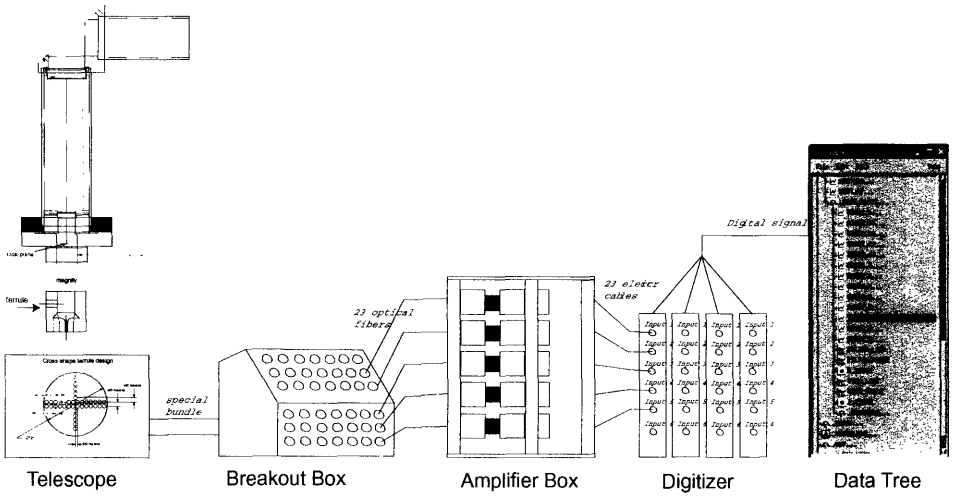

Figure 2-4: System overview of the outboard fast photodiode diagnostic system

Fig. 2-4 gives a schematic overview including all the main components. The central part of the system is the 23-channel detector and amplifier box. Each channel is equipped with a pair of variable aperture optical lenses, a filter holder and an interference filter. The filters used are fitted tightly in between the pairs of lenses. Each combination of lenses and filter is always used with the same diode since minor differences in their filter functions are possible.

2.4 Telescope and ferrule geometry

On the left side of 2-4, the viewing telescope and a cylindrical ferrule shown in red and positioned by the ferrule holder at the bottom of the telescope are depicted. The

telescope was designed to produce a minimal spot size of an object located just in front of the gas puff nozzle, in the plane where the ferrule connects to the telescope.

The RMS spot size is calculated by tracing 32 exact rays through the optical system from the center field point and measuring the standard deviation of the positions at which the rays intersect the image surface. The optical rays were set to the D_α wavelength and the Lobatto quadrature sampling method was used to pick rays that go through different aperture points.[13]

The set screws installed between the bottom of telescope flange and the top of the ferrule holder enables fine focusing of the telescope.

The telescope was designed using optics optimization software OSLO and is based on former versions of telescopes used in Alcator C-Mod. The optics consists of a flat mirror, shown in red on Fig. 2-4 and two doublets. The front doublet (MGLA 139) has a diameter of 30 mm and is located 118 mm from the second doublet (MGLA 47) of 14 mm diameter. The doublets are positioned using Teflon lens holders and stainless steel spacers. To minimize eddy currents in the cylindrical lens spacer of 118 mm total length, it was sliced into four shorter parts of equal diameter.

Effective focal length	99.45 mm
Numerical aperture	0.1942
Working F-number	2.574
Lateral magnification	-0.1266
RMS spot size at center	0.0363 mm

Table 2.2: Optical parameters for the outboard viewing telescope used by the fast photodiode system. The RMS spot-size is for a point object.

The ferrule geometry with both front and top view is shown again but in greater detail in Fig. 2-5. The circular form shown in the front view is the end plane of the ferrule which is placed in the focal plane of the telescope. The object (plasma edge) is imaged onto the plane. The tiny circles are the individual fiber ends with diameters of 400 microns. To enhance the imaging resolution at the radial location near the separatrix, two normal fibers are replaced with four mini fibers of diameters of 200 microns.

These fibers then continue tightly bound together and break out outside the vessel in a specially designed box also shown in Fig. 2-4.

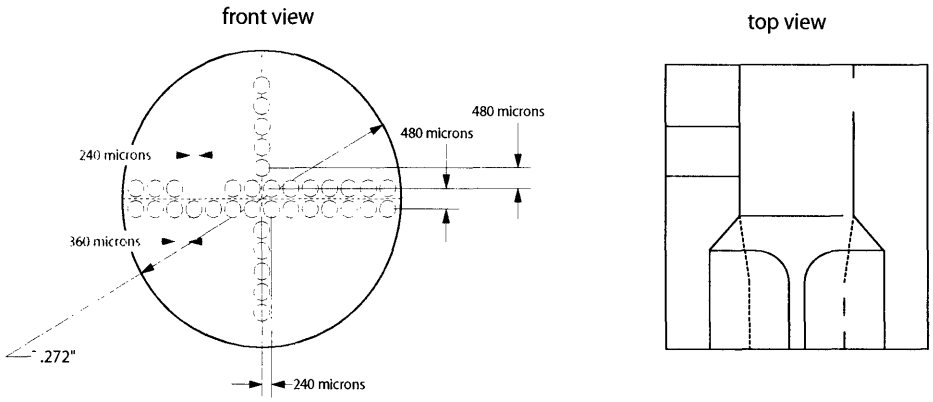

Figure 2-5: Ferrule geometry

2.5 SD-100 photodiode and amplifier circuit

The measurement of emission fluctuations near the plasma edge benefits from using photodiodes with high quantum efficiency at wavelengths near 656 nm. These diodes have been successfully used by R. J. Fonck [10] combined with an extremely low-noise preamplifier and a reactive feedback circuit.

Fonck showed that the photodiode-amplifier combination yielded a non-electronics-noise-limited response down to ~1 nW, and that the photon-noise level at ~20 nW was 14 and 4 times lower than those of other possible detector systems, photo-multipliers and avalanche photodiodes respectively. Of course the use of the high-sensitivity photodiodes required the use of a high gain, low noise amplifier circuit that has good frequency response over the range of frequencies of interest, 0 to ~200 kHz. This is provided by the circuit described by Fonck. Essentially it consists of a very high-gain trans-impedance section (3×10^8 V/A). Since this section has a strong

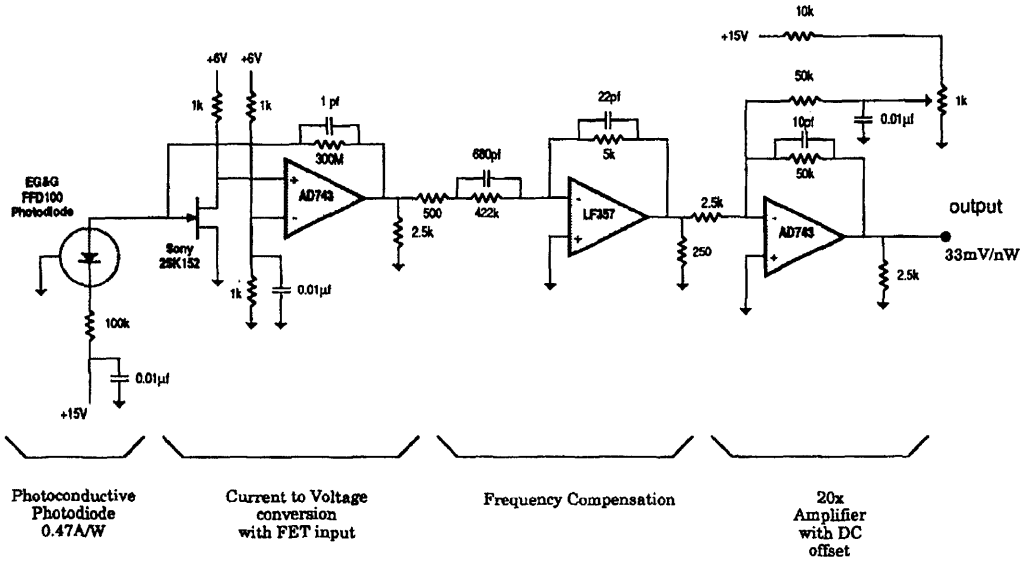

Figure 2-6: Diagram of the photodiode amplifier circuit

roll-off of gain with frequency, it is followed by a section, essentially a differentiator section, that compensates almost exactly the frequency roll-off. This compensation section is then followed by a $\times 20$ voltage-to-voltage amplifier. This circuit is used by most beam emission spectroscopy (BES) measurements on tokamaks and can be used with actively cooled detectors if even lower signal levels are of interest. It has the disadvantage, however, of a limited dynamic range, $\sim$50 mV to $\sim$2 V, where the upper limit is a result of 1st stage reaching the power supply voltage limit (V_{cc}) at low frequencies. Thus for the work described here, the dynamic range of the entire system is provided by manually adjusting the f-numbers of the lens apertures in the coupling of the fiber inputs to the detectors.

The chosen photodiode is the SD 100-11-31-221 PIN photodiode detector from Advanced Photonix Inc. as shown on Fig. 2-7. It has an active area of 5.1 mm^2.

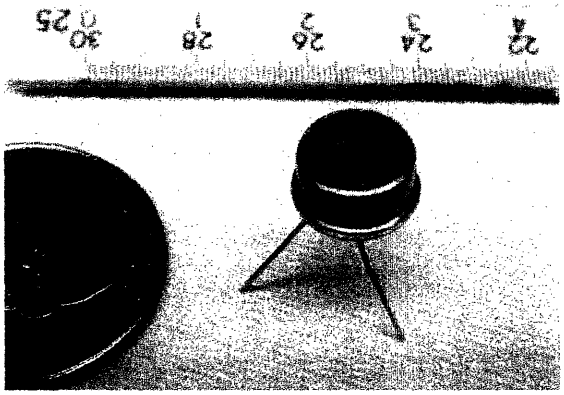

Figure 2-7: The SD 100 diode has a quantum efficiency of 0.8 at 656 nm and a sensitivity of roughly 0.45 A/W.

2.6 Absolute sensitivity calibration of the photodiodes

In order to determine the absolute brightness of the plasma, we have placed an extended light source with known intensity inside the vessel during maintenance period. While the in vessel telescopes are collecting light from the calibration light source, the voltage read out is recorded. Later, based on simple proportionality, the brightness of a discharge will be known from the photodiode read out (see Fig. 2-8).

The photodiode modules transform the incoming optical signal measured in units of watts of total incident power (P_{in}) to units of volts of electrical signal (V_{out}). We define sensitivity (S) as the proportionality factor between these two quantities. S is not just a property of the photodiode, but of the entire diagnostic system between the light source and the photodiode, including the photodiode amplifier circuit.

$$V_{out} = SP_{in}. \tag{2.1}$$

We characterize the source of light by the brightness function $B(\lambda)$. We assume that the brightness has no dependence on the direction and has units of μ W/cm^2/st/nm. We now expand Eq. (2.1) to get

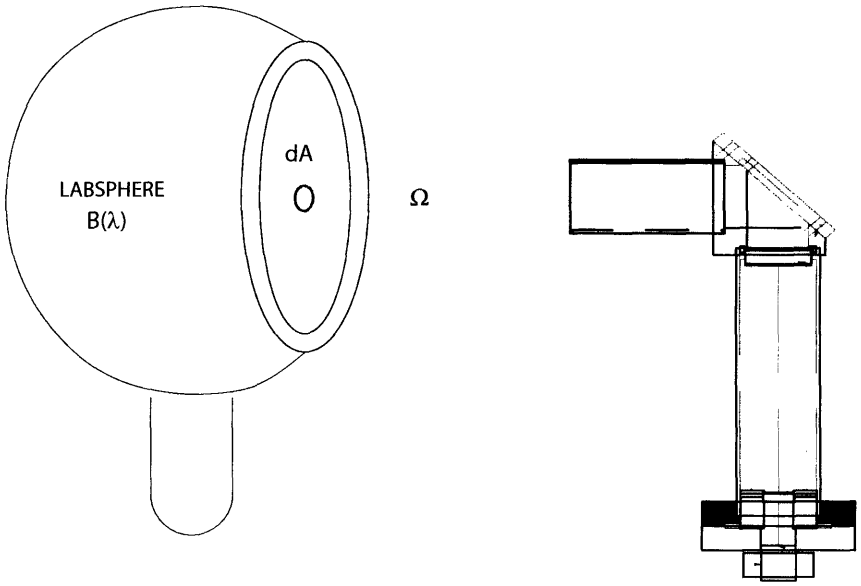

Figure 2-8: The schematic outline shows the setup used for the labsphere calibration. The above calibration took place inside the vessel with the telescope mounted to position.

$$V_{out} = S(\lambda) \int \int B(\lambda)\Omega(A)\, dA\, d\lambda. \tag{2.2}$$

The D_α bandpass filter installed in front of the photodiodes makes $S(\lambda)$ independent of λ. We account for it by introducing the filter function T_f, and S'

$$V_{out} = S' \int \int B(\lambda)T_f(\lambda)\Omega(A)\, dA\, d\lambda. \tag{2.3}$$

Since the individual fiber areas are small compared to the distance from the focal plane to the telescope, we can replace $\int dA$ by ΔA. We can also approximate $\Omega \approx A_t/l^2$, where A_t is the total area of the primary lens of the telescope and l is the distance between the focal plane and the primary lens. Evaluating the area integral in the telescope focal plane we get

$$V_{out} = S' \frac{A_t}{l^2} \int B(\lambda)T_f(\lambda)\, d\lambda. \tag{2.4}$$

By performing the calibration with the Labsphere, a calibrated source, and by

taking a real plasma shot with all the other settings the same, i.e. same transfer fiber, same f-number setting for the lenses in the detector and amplifier box, we have two instances of Eq. (2.4), one containing the Labsphere brightness $B_{Labsphere}$, the second one containing the plasma brightness B_{plasma}

$$V_{Labsphere} = S' \frac{A_t}{l^2} \int B_{Labsphere}(\lambda) T_f(\lambda)\, d\lambda \tag{2.5}$$

$$V_{plasma} = S' \frac{A_t}{l^2} \int B_{plasma}(\lambda) T_f(\lambda)\, d\lambda. \tag{2.6}$$

After dividing Eq. (2.6) by Eq. (2.5) and rearranging, we have

$$\int B_{plasma}(\lambda) T_f(\lambda)\, d\lambda = \frac{V_{plasma}}{V_{Labsphere}} \int B_{Labsphere}(\lambda) T_f\, d\lambda. \tag{2.7}$$

We furthermore assume that in the ~10 nm bandwidth around the D_α line, the plasma is only emitting at D_α. We can then write

$$\int B_{plasma}(\lambda) T_f(\lambda)\, d\lambda = \int B_{plasma}(\lambda)\, d\lambda \int T_f(\lambda) \delta(\lambda - 656.1nm)\, d\lambda \tag{2.8}$$

Finally, assuming that the plasma brightness is due to a plane light source, we have

$$B_{plasma}(\lambda \to 656.1 \text{ nm})[\mu W/cm^2/st] = \frac{V_{plasma}}{V_{Labsphere}} \frac{\int B_{Labsphere}(\lambda) T_f(\lambda)\, d\lambda}{T_f(\lambda \to 656.1nm)}. \tag{2.9}$$

2.6.1 Labsphere continuum spectrum and filter function

For the laboratory calibration the URS-600 UV-enhanced labsphere was used. The intensity versus wavelength of the labsphere is shown in Figure 2-9.

The transmission of the band pass filter provided by the Andover Corporation centered around D_α is plotted against wavelength in Figure 2-10.

Using the labsphere brightness profile and the filter function it is now possible to

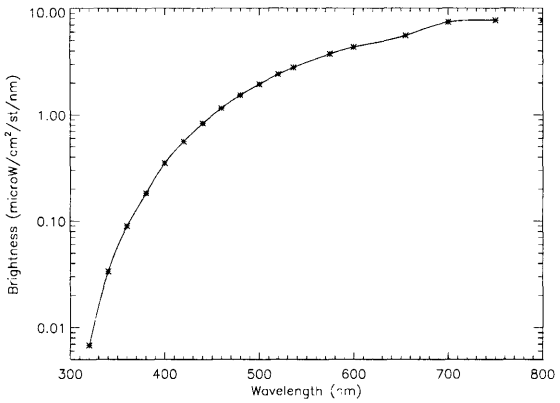

Figure 2-9: The brightness profile of labsphere URS-600 for the labsphere monitor diode reading of 728 ft lamberts. The actual brightness has to be scaled by the actual labsphere monitor diode reading.

evaluate the $\int B_l(\lambda)T_f(\lambda)\,d\lambda$ term in Eq. (2.7). The used code including the data series for the filter function and the labsphere profile is in appendix A.

2.7 Relative calibration of views and transmission fibers

In the previous section the sensitivity of the fast photodiode system was documented. This calibration description was simplified for brevity, as if one view would always be used with one transfer fiber and with one detector/amplifier box. In fact, we desire to couple any of the possible views to any of the detector/amplifier boxes using any of the available transfer fibers. The transmissions of the different transfer fibers were measured and are given in the following table (see Table 2.7). A transmission of 1.000 would be a perfect transmission without losses.

The relative transmission of the views, including the collecting efficiency of the telescope and the fiber areas, as well as the fiber transmission up to the breakout-box, are given in Table 2.7.

Similarly, the relative sensitivity of the photodiode amplifier circuits are also given in Table 2.7. Here, diode # 1 is the reference diode.

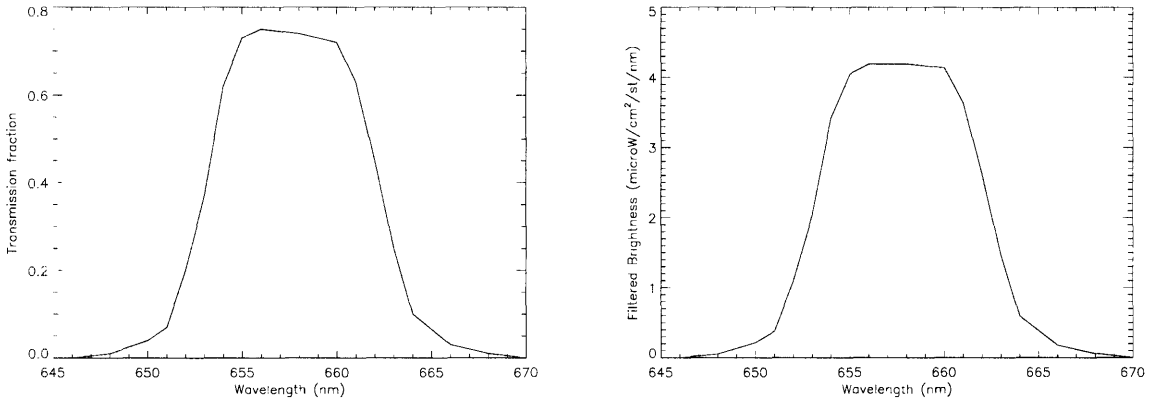

(a) (b)

Figure 2-10: (a) shows the transmission profile of the D_α filter, SN K122-06, installed on diode 7. (b) depicts the filtered brightness profile for the labsphere calibration.

2.8 Signal control and processing

The availability of digital signal processors and digital data storage has greatly transformed plasma diagnostics over the past decades. Each of the 23 channels records a time series of 2^{17} to 2^{19} data samples during each shot, an easy task for the C-Mod data acquisition system. In addition to the output signals from the photodiode amplifier circuits, one needs to record all the properties associated with the recorded fluctuation signal, for example the corresponding view, its calibration factors, etc.

When the former 13 channel system was updated to the current 23 channel one, the data structure was redesigned. Among the design principles was easy maintainability, compatibility with the older codes based on the old data structure, re-usability and simplicity.

As shown in Fig. 2-11 all the property data were structured into three different levels, *unordered arrays*, *ordered arrays* and *signal properties* . The unordered arrays contain all possible hardware choices for example all possible transfer fibers or all possible views. These unordered arrays are only extended when a new hardware addition is made. These are:

1. available f-numbers

Transfer fiber	Transmission
GPI #1	0.763
GPI #2	0.676
GPI #3	0.727
GPI #4	0.681
GPI #5	0.738
#20	0.760
#21	0.766
#22	0.634
#26	0.760
#39	0.709
#40	0.741
#41	0.740
#42	0.749
#43	0.734
#44	0.745
#45	0.753
#46	0.708
#47	0.735
#48	0.739
#49	0.754
#50	0.713
#51	0.763
#52	0.753

Table 2.3: Transmission of the transfer fibers.

2. available view labels
3. available radial locations of the focal spots of the views
4. available vertical locations of the focal spots of the views
5. available transfer fiber labels
6. available feed-through fiber numbers
7. available interference filters.

The ordered arrays contain those properties associated with each of the 23 measurements. Thus each element in an ordered array is associated with one of the presently 23 diode detectors. We choose to assign element # 1 to diode detector # 1, element # 2 to diode # 2, and so on.

Every time a transfer fiber is used with a different detector or another of the possible views is used with a given detector then a change is made to the ordered arrays. These ordered arrays have a length of 23, which is the current number of detectors. These arrays are:

1. view number
2. view name
3. view transmission coefficient
4. radial position of the view
5. vertical position of the view
6. f-number used with the given detector box
7. relative transmission with the f-number of the detector box
8. transfer fiber
9. transmission of the transfer fiber
10. feed-through fiber
11. transmission of the feed-through fiber
12. filter
13. absolute sensitivity

Lastly, to enable a user to directly open up the tree using traverser and immediately see the properties associated with a certain signal, the following string, integer or floating variables are dynamically generated from the unordered and ordered arrays. While there is only one instance of the ordered and unordered arrays, there are exactly 23 instances of these variables. These variables are:

1. view number of the given signal
2. radial position of the given signal
3. vertical position of the given signal

4. transfer fiber of the given signal
5. transmission of the transfer fiber of the given signal
6. relative sensitivity of the given signal
7. f-number used with the given detector box
8. feed-through of the given signal
9. feed-through coupler of the given signal
10. transmission of the feed-through coupler of the given signal
11. master calibration of the given signal

View	Transmission
OUTER SOL 1	0.312
OUTER SOL 2	0.392
OUTER SOL 3	0.383
OUTER SOL 4	0.118
OUTER SOL 5	0.110
OUTER SOL 6	0.110
OUTER SOL 7	0.093
OUTER SOL 8	0.000
OUTER SOL 9	0.409
OUTER SOL 10	0.407
OUTER SOL 11	0.430
OUTER SOL 12	0.441
OUTER SOL 13	0.409
OUTER SOL 14	0.406
OUTER SOL 15	0.099
OUTER SOL 16	0.147
OUTER SOL 17	0.368
OUTER SOL 18	0.326
OUTER SOL 19	0.428
OUTER SOL 20	0.437
OUTER SOL 21	0.458
OUTER SOL 22	0.318
OUTER SOL 23	0.471
OUTER SOL 24	0.368
OUTER SOL 25	0.383
OUTER SOL 26	0.342
OUTER SOL 27	0.419
OUTER SOL 28	0.192
OUTER SOL 29	0.365
OUTER SOL 30	0.285
OUTER SOL 31	0.366
OUTER SOL 32	0.390
OUTER SOL 33	0.434
OUTER SOL 34	0.447
OUTER SOL 35	0.473
OUTER SOL 36	0.435
OUTER SOL 37	0.356
OUTER SOL 38	0.347
OUTER SOL 39	0.450
OUTER SOL 40	0.405
Inner SOL A	0.213
Inner SOL B	0.233
Inner SOL C	0.206
Inner SOL D	0.224
Inner SOL E	0.204
Inner SOL F	0.262

Table 2.4: Relative transmission of the views

Diode #	Relative sensitivity
1	1.000
2	0.964
3	0.893
4	1.206
5	1.321
6	1.363
7	1.300
8	1.363
9	1.276
10	1.225
11	1.139
12	1.148
13	1.197
14	0.945
15	0.982
16	0.900
17	0.784
18	0.755
19	0.762
20	0.721
21	0.827
22	0.870
23	0.766

Table 2.5: Relative diode sensitivities

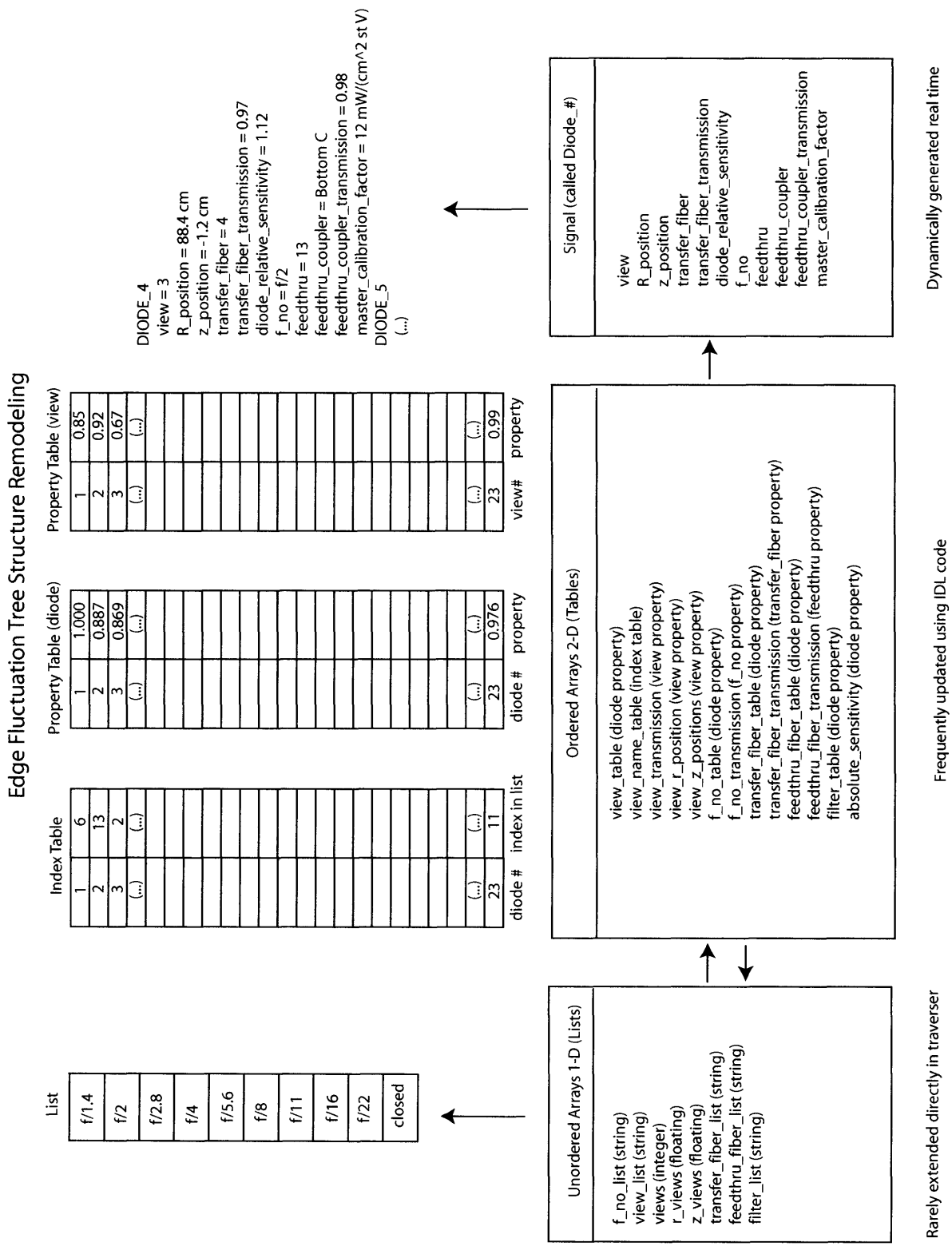

Figure 2-11: Schematic data structure of the photodiodes tree

Chapter 3

Analysis and results

3.1 Overview of the plasma discharges analyzed

In order to study three main topics,

1. Outboard steady-state D_α emission profiles with and without a local D_2 gas puff

2. Inboard vs. outboard steady state D_α emission profiles in L and H-mode

3. D_α emission spatial and temporal fluctuations on the outboard plasma edge

a number of plasma discharges from Alcator C-Mod were analyzed. Table 3.1 has a summary of the most frequently referred to shots. The shot numbers that are described as cycle test or fizzle are used for offset voltage subtraction. One tries to choose the background shot as close in time to the real plasma shot as possible in order to eliminate any effects of longtime scale drifts in offsets due to the temperature change of the amplifier circuit.

All of the discharges analyzed took place in the spring and summer of 2005, except for shot 1031204007 that was taken with the old 13-channel system before the upgrade to the current 23-channel system in January 2005.

Shot number	Discharge	NINJA gas puff trigger	Diode trigger
1031204001	cycle test	no puff	used for background
1031204007	plasma	no puff	0.7 s
1050303001	fizzle	no puff	used for background
1050303005	plasma	A-B limiter at 0.5 s	0.55 s
1050304006	plasma	A-B limiter at 1.0 s	1.05 s
1050304007	plasma	A-B limiter at 1.0 s	1.16 s
1050304008	plasma	A-B limiter at 1.0 s	1.16 s
1050304012	plasma	A-B limiter at 1.0 s	1.16 s
1050304028	fizzle	no puff	used for background
1050603013	plasma	no puff	0.65 s
1050603027	fizzle	no puff	used for background
1050628002	plasma	A-B limiter at 0.58 s	0.70
1050628006	fizzle	no puff	used for background

Table 3.1: Summary of the most frequently referred to plasma discharges

3.2 Absolute brightness profile of D_α

The absolute calibration of the diagnostic enables direct measurement of the D_α brightness in units of W/cm^2/ster. The viewing area of the in-vessel view telescope is fixed, but the radial location of the last closed magnetic surface (LCMS or separatrix) varies somewhat with time, and can be different from discharge to discharge or even within a discharge.

For a more generic interpretation, we are interested in plotting the absolute brightness profile relative to the position of the separatrix. The position of the separatrix is calculated using EFIT. EFIT is a code based on the measurements of many magnetic coils that computes the equilibrium magnetic field and plasma current.

The error in the brightness measurements is obtained by cumulatively calculating the error from each measurement that is used in its determination. The largest source of error arises from the reproducibility of the optical apertures of the input lenses in the detector boxes. Ideally, the area of the opening of a lens increases by a factor of two every time the f-number is changed to the next position. Due the angular distribution of light exiting the fiber, the geometry of the lens holder and the attached fiber connector, the amount of light reaching the photodiodes does not,

Aperture change	Scaling factor [1]	Relative error
f/1.4 to f/2	1.161	0.026
f/2 to f/2.8	2.158	0.049
f/2.8 to f/4	4.264	0.061
f/4 to f/5.6	8.276	0.078
f/5.6 to f/8	15.75	0.091
f/8 to f/11	28.63	0.122
f/11 to f/16	54.20	0.142

Table 3.2: Relative error at different aperture settings based on diode 18

in reality, change by a factor of two between adjacent f-number settings. Table 3.2 shows the decrease in transmission relative to f/1.4, the scaling factor, as well as the relative error based on five series of calibrations.

The relative error is larger for smaller apertures. This is due to the fact that errors propagate when going to higher scaling factors. Let

$$z = x^m \tag{3.1}$$

then the simple average error is given by,

$$\frac{\Delta z}{z} = |m|\frac{\Delta x}{x} + \ldots. \tag{3.2}$$

The geometry of the active views for shot 1050304012 is shown in Figure 3-1. The inboard views were recorded by using the inboard SOL viewing telescope, which was calibrated in the same way by placing the Labsphere inside the tokamak. The center of the cross-shaped viewing geometry is usually just outside the separatrix.

3.3 D_α emission profiles using gas puff

One of the problems with these line integrated optical measurements is the presence of plasma behind and in front of the gas-puffing plane (see Fig. 3-3). In this technique the gas puff is used to toroidally localize the measurement of the edge plasma properties by increasing the level of D_α intensity above the intrinsic chord-integrated

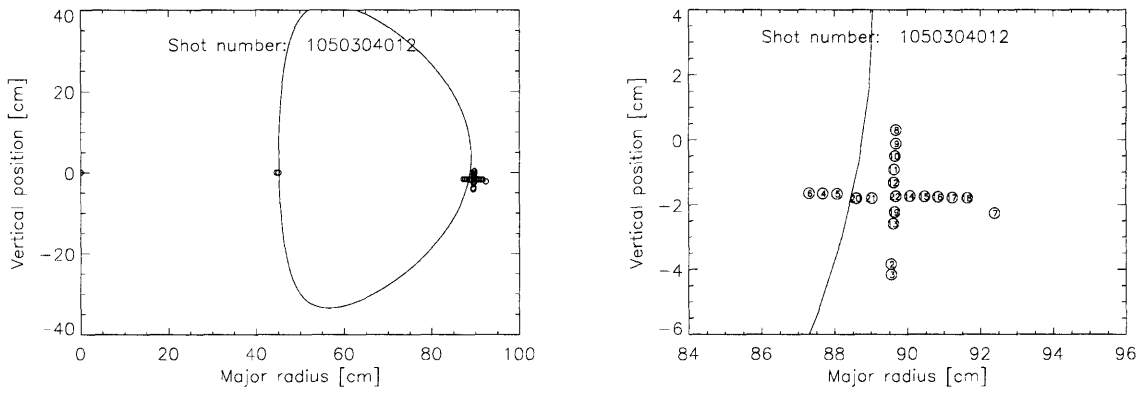

(a) (b)

Figure 3-1: (a) and (b) show the geometry of the active views.

brightness by factors of 3 to 20.

To monitor the process of the neutral D_2 reaching the plasma as puffed from between the upper and lower array of tiles of the A-B limiter, we select a single view from two different shots, where the photodiodes capture the process of the puffed gas reaching the viewed region (shot 1050303005 and 1050628002) as shown in Figure 3-2.

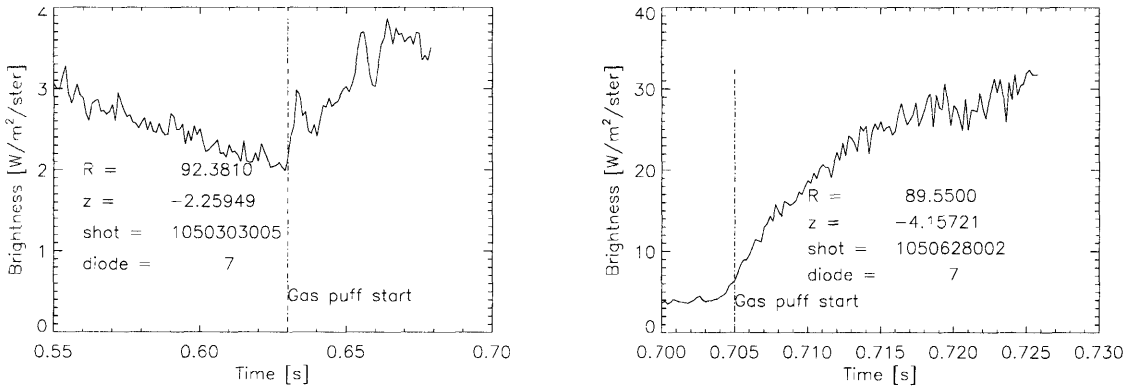

Figure 3-2: The brightness increases sharply as the the D_2 puff reaches the plasma. NOTE: (a) and (b) are plotted on different time scales.

The exact shape of the neutral gas puff is unknown, but in this section we estimate its spatial extent based on the amount of increase in D_α brightness.

It is now possible to take averages of the local plasma brightnesses right before

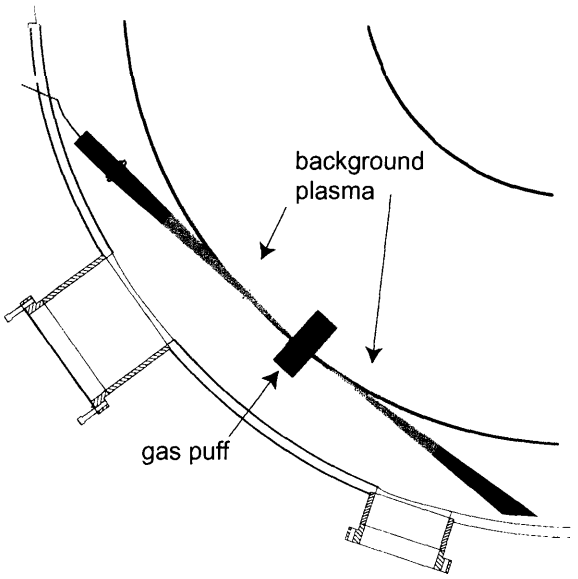

Figure 3-3: Schematic top view of the outboard viewing telescope and neutral gas puff. Note that in reality the background plasma D_α emission, shown here as a rectangle, is in fact an approximately toroidally symmetric shell of emission, localized to the separatrix region. The rectangular extent of the gas puff is also only schematic.

and after the gas puff. The difference in the intensity taken from before and after the gas puff should give the D_α brightness due to the gas puff. The two steady state periods of time from before and after the gas-puff are selected so that they are as close in time as possible, since as seen in later sections, different modes of operations have different brightness profiles.

3.3.1 Radial brightness profile of 1050303005

On shot 1050303005 the gas puff starts to affect the D_α brightness at $t = 0.63$ s. Therefore, the pre-gas puff steady state profile is averaged over $t_{nopuff} = [0.61s, 0.63s]$. The post gas puff steady state profile is plotted over $t_{gas} = [0.66s, 0.68s]$. The before and after the gas puff steady state D_α brightness profiles are plotted on the same scale as shown in Fig. 3-4.

Now, one can simply take the difference of the two profiles from before and after the gas puff. The radial profile of the D_α emission due to the gas puff is given in Fig. 3-5.

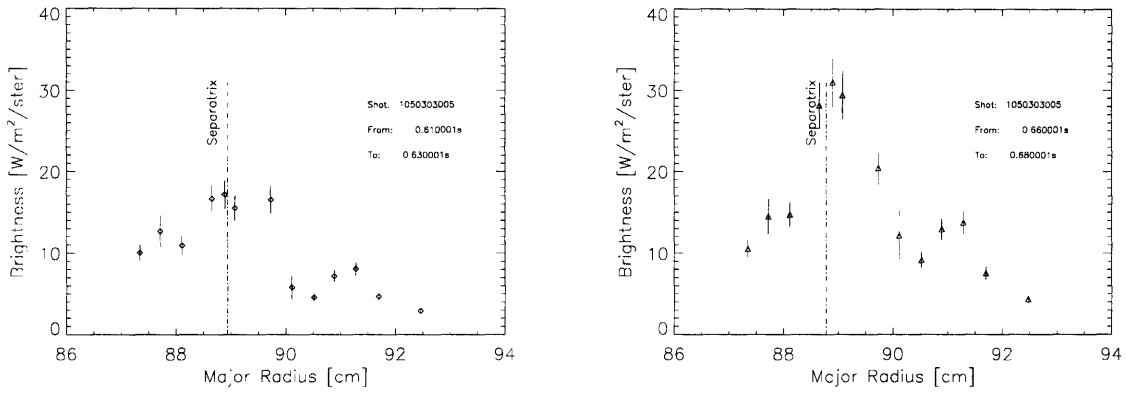

(a) (b)

Figure 3-4: (a) before the gas puff (b) after the gas puff. The x-axis is the major radius of the view as if the actual r and z coordinates were projected to the midplane along the flux surface.

3.3.2 Radial brightness profile of 1050628002

The edge brightness increases more dramatically after the gas puff on shot 1050628002. As Fig. 3-2 (b) shows, there is just enough period of pre-puff signal for building a time averaged steady state profile. Fig. 3-2 (b) also shows that the time required for the gas puff to reach its maximum effect on the emission is $\sim$ 20 ms.

Since the emission for the puff was significantly higher and since the background without the gas puff was lower than the pre-puff profile of shot 1050303005, the subtracted brightness profile has smaller error bars on Fig. 3-7. Note that the total amount of D_2 puffed in the cases was 7.3 Torr·liters for 1050303005 and 5.4 Torr·liters for 1050628002.

3.3.3 Poloidal brightness profile of 1050303005

In the same fashion, the poloidal D_α brightness profile is also measured before and after the gas puff as shown in Fig. 3-8.

If one accepts the assumption that the electron temperature and the density profiles are constant on a flux surface to first order, the poloidal brightness profile of the intrinsic D_α emission should be approximately constant, since the different views in

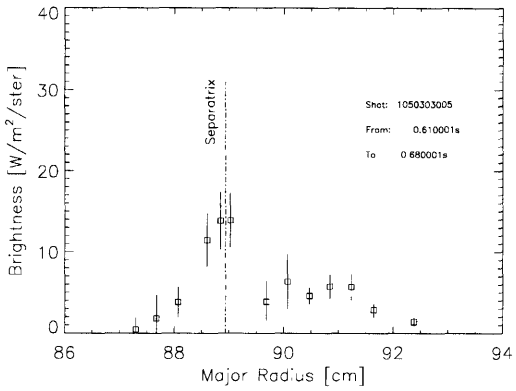

Figure 3-5: The difference between the brightness profiles before and after the gas puff is purely the result of the D_2 puff.

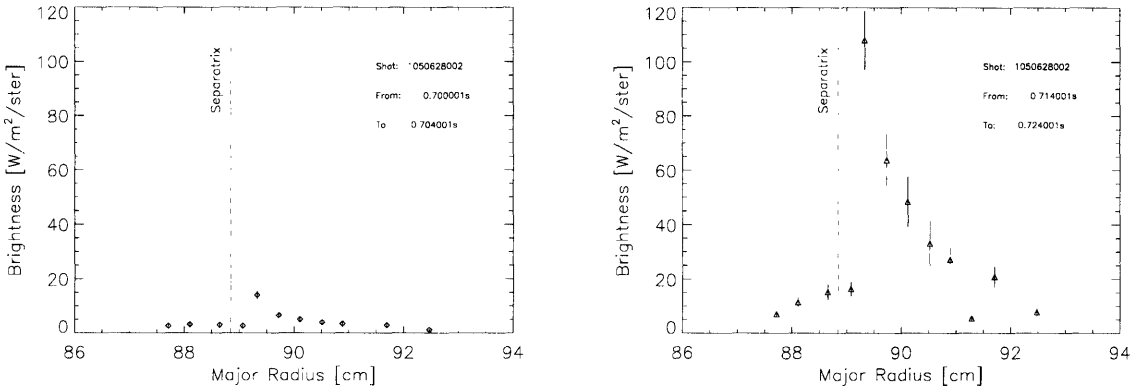

(a) (b)

Figure 3-6: (a) before the gas puff (b) after the gas puff

the poloidally resolving group have minor radii that differ by a maximum of 3.8 mm due to the curvature of the flux surfaces (see Fig. 3-1 (b)).

The difference of the profile of the brightness before and after the gas puff gives the poloidal profile due to the gas puff in Fig. 3-9.

3.3.4 Approximating the vertical extent of the gas puff

The exact shape and 3-D neutral density profile of the gas cloud puffed into the SOL is unknown. The four-channel puffing nozzle is assumed to produce a shock wave

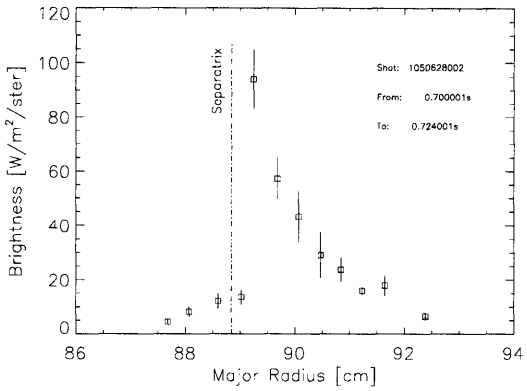

Figure 3-7: The difference between the brightness profiles before and after the gas puff peaks near the separatrix.

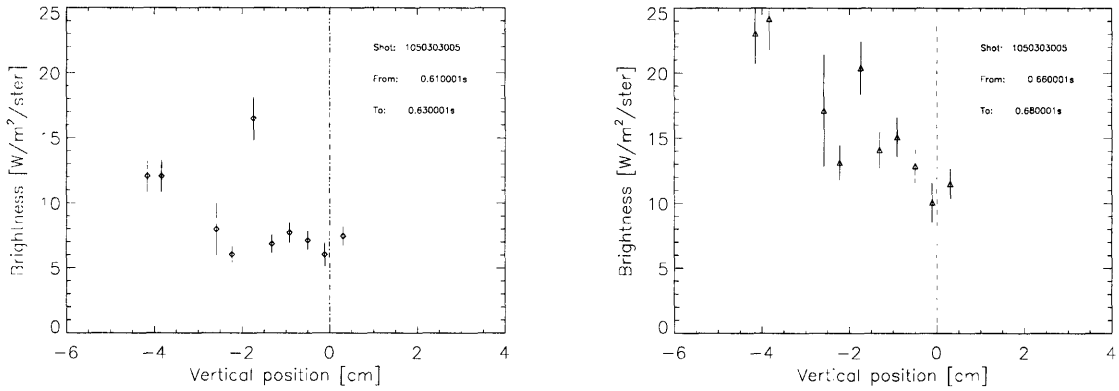

(a) (b)

Figure 3-8: (a) before the gas puff (b) after the gas puff

free, laminar flow into the SOL. The vertical positions of the nozzles are known, the center of the four-channel-array is located at $z = -2.5$ cm. The vertical extent of the D_α emission, and thus the gas puff, can be estimated using the poloidal array of views. Furthermore, we assume that the toroidal extent of the puff is similar to the vertical, then the toroidal extent can be estimated as well. This is important because it impacts the radial resolution of the fluctuation measurements.

The radial extent of the gas puff is important, since one wants to use this technique to measure fluctuations as far inside as possible.

The poloidal extent of the gas puff and thus the upper limit on the toroidal extent

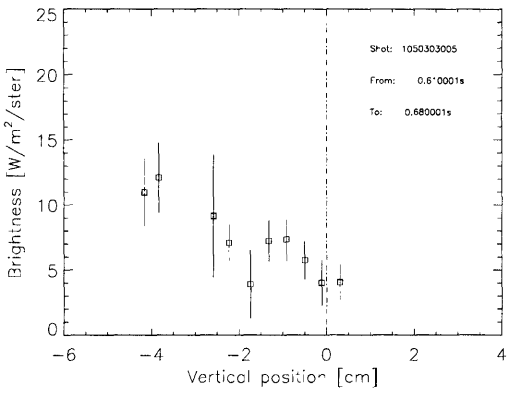

Figure 3-9: The poloidal profile is higher for lower locations.

can now be estimated based on Fig. 3-9. If we assume that the poloidal profile peaks at and is symmetric about the measurement at -3.8 cm vertical position, then the Half-Width-Half-Maximum (HWHM) of the vertical extent of the gas cloud is ~2.5 cm, yielding a FWHM of 5 cm. This is obviously only an approximate measurement.

3.4 Intrinsic D_α profiles without gas puffing

The measurements using the D_2 gas puff yield information about the gas puff itself, but it tells nothing about the unperturbed D_α brightness profile of the plasma edge region.

Shot 1050603013 is now analyzed to yield the intrinsic brightness profile without a gas puff. This shot has the least absolute error compared to the other analyzed shots since the apertures are wide open on all of the views for this shot.

3.4.1 Radial D_α emissivity with Abel inversion

Recall that without the gas puff, the D_α brightness that the photodiode diagnostic measures is the chord integrated intrinsic D_α emissivity that is reasonably assumed to be toroidally symmetric. Using the assumption of toroidal symmetry, one can Abel invert the brightness profile to obtain the radial profile of the emissivity..

Using the notations of Abel inversion from Hutchinson [14], the measured quantity $F(y)$ is the line integral of the local plasma property $f(y)$,

$$F(y) = \int_{-\sqrt{a^2-y^2}}^{+\sqrt{a^2-y^2}} f(r)\, dx \tag{3.3}$$

where a is the maximum major radius of emission, x is the length of the chord, and y is the distance between the chord and the center of the symmetry. After changing into an integral over r (distance from the center) and inverting the integral equation involving $f(r)$,

$$f(r) = -\frac{1}{\pi}\int_r^a \frac{dF}{dy}\frac{dy}{\sqrt{y^2-r^2}} \tag{3.4}$$

and defining ϵ as the emissivity at D_α, and using $B(y)$ for D_α brightness, we have

$$\epsilon(r) = -\frac{1}{\pi}\int_r^a \frac{dB}{dy}\frac{dy}{\sqrt{y^2-r^2}}. \tag{3.5}$$

In our case of deducing $\epsilon(r)$, the assumption of parallel chords has to be made. Since the distance to the viewing telescope is many times larger than distance between the furthest views, we assume the case of parallel chords.

Due to the errors and uncertainties of $B(y)$, dB/dy is not a very well defined property, so we chose to fit the brightness profile with a Gaussian function in the form of

$$f(x) = A_0 e^{-\frac{1}{2}(\frac{x-A_1}{A_2})^2} + A_3 + A_4 x + A_5 x^2. \tag{3.6}$$

Fig. 3-10 depicts the original D_α brightness profile as well as the Abel inverted D_α emissivity.

Error bars on the emissivity profile are not shown, nevertheless, errors in the emissivity profile are obviously greater than those in the brightness profile.

The inversion of the inboard D_α brightness requires more care, since the inboard viewing telescope collects light from the outboard plasma edge region. Luckily, once we know the outboard D_α emissivity (Fig. 3-10), this emissivity can be line inte-

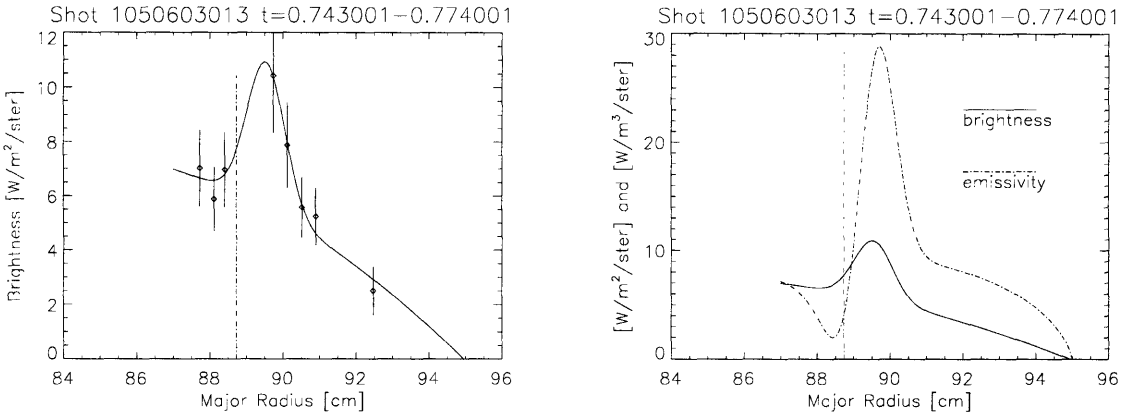

Figure 3-10: (a) D_α outboard brightness profile showing error bars and Gaussian fit and (b) Fitted brightness and Abel inverted outboard emissivity

grated and the outboard contribution can be subtracted from the observed inboard D_α brightness profile.

Fig. 3-11 depicts the inboard D_α brightness and emissivity profiles. The inboard radial coordinates are transformed to midplane outboard radial coordinates so that the inboard and outboard D_α profiles can be easily compared.

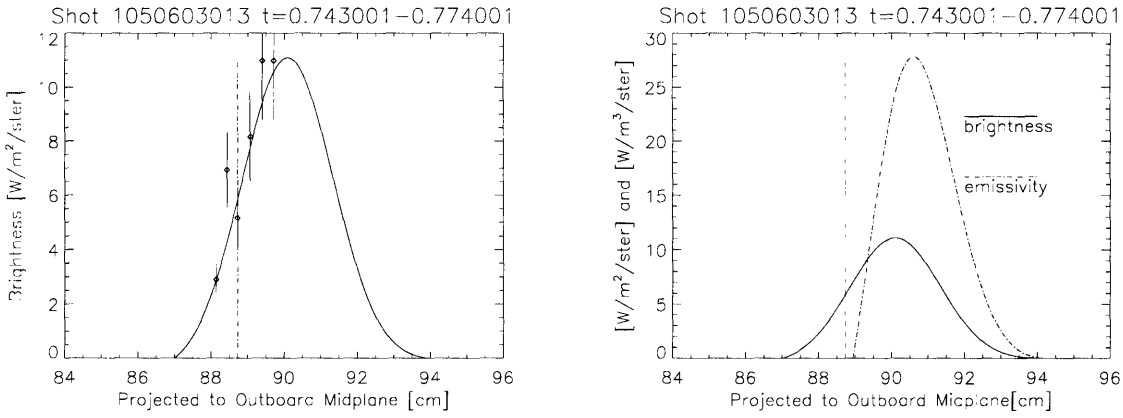

Figure 3-11: (a) D_α inboard brightness profile showing error bars and Gaussian fit and (b) Fitted brightness and Abel inverted inboard emissivity

3.5 L-mode and H-mode D_α profiles without gas puffing

In the following sections, L and H mode steady state D_α profiles are compared in three situations,

1. D_α radial outboard profiles
2. D_α radial inboard profiles
3. D_α poloidal outboard profiles

The L and H modes have been long known as the two different levels of confinement in recent tokamaks. Without placing an emphasis on this comparison, the intrinsic uninverted D_α brightness profiles are given in the following subsections. For each of the following three cases, the steady state profiles have been averaged over the time periods shown in Fig. 3-12 without further analysis.

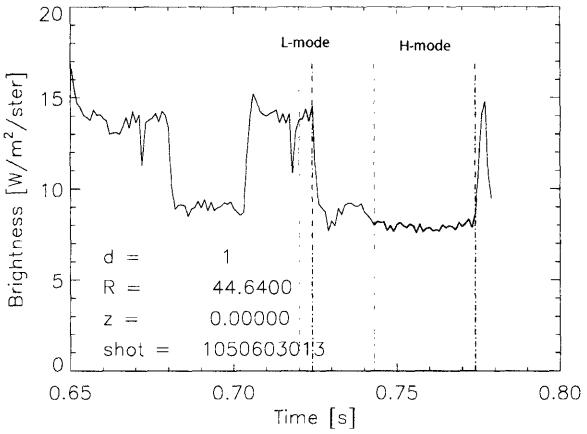

Figure 3-12: The L-mode and H-mode periods that were selected for the profile measurement.

3.5.1 L-mode and H-mode D_α radial outboard profiles

The L and H-mode radial outboard D_α profiles are shown in 3-13.

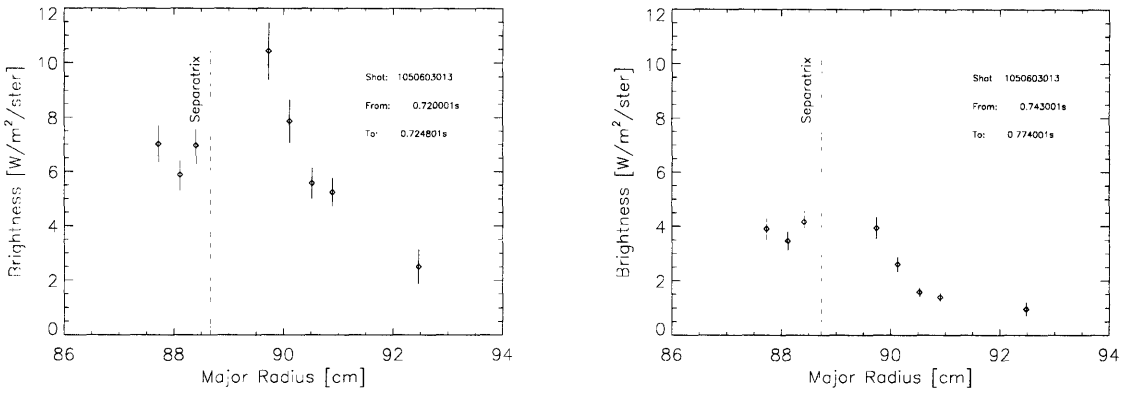

L-mode H-mode

Figure 3-13: Radial outboard profile

3.5.2 L-mode and H-mode D_α radial inboard profiles

The L and H-mode radial inboard D_α profiles are shown in 3-14. Since the major radii corresponding to the inboard views range from $R = 44.24$ cm to $R = 46.23$ cm, the major radii are projected on the outer midplane using the corresponding flux surface. Therefore, the inboard profiles will also be plotted on the same major radius range as the outboard profiles.

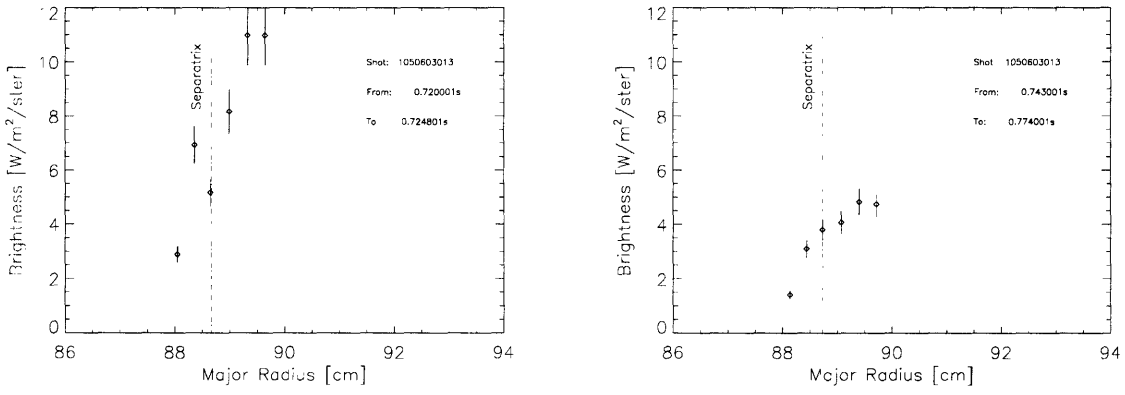

L-mode H-mode

Figure 3-14: Radial inboard profiles. The radial inboard coordinates are projected onto the outboard midplane along the flux surfaces to help comparison.

It is important to note that as Fig. 2-2 shows the inboard views look through the

same D_α emission region at the outboard edge as measured by the outboard telescope.

3.5.3 L-mode and H-mode D_α poloidal outboard profiles

The L and H-mode poloidal outboard D_α profiles are shown in 3-15.

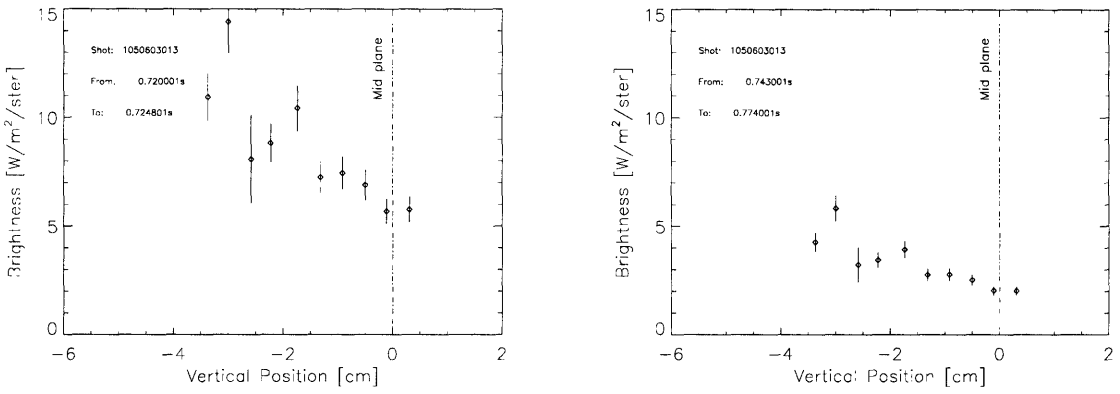

L-mode H-mode

Figure 3-15: Poloidal outboard profile

3.6 Statistical description of D_α intensity fluctuations

One of the most distinctive properties of the fast photodiodes diagnostic is the high temporal resolution. At each spatial location, a time series of at least 131,071 (2^{17}) data points are recorded, some views recorded by a more recent digitizer can store up to four times (2^{19}). The frequency of digitization is 1 Mhz, so that the minimum total time span of the measurement is around 0.131 s.

This makes it possible to use statistical tools to analyze the plasma brightness fluctuations. Due to the propagation of errors arising from the several steps of calibrations, the absolute measurements are limited to a large extent. Brightness fluctuations, however, rely on the quantity $\frac{\tilde{n}}{n}$ rather than n itself, and thus the absolute errors are canceled.

Mean	$\bar{x} = \frac{1}{N}\sum_{j=0}^{N-1} x_j$
Variance	$\sigma^2 = \frac{1}{1-N}\sum_{j=0}^{N-1}(x_j - \bar{x})^2$
Standard Deviation	$\sigma = \sqrt{\frac{1}{1-N}\sum_{j=0}^{N-1}(x_j - \bar{x})^2}$
Skewness	$s = \frac{1}{N}\sum_{j=0}^{N-1}(\frac{x_j - \bar{x}}{\sigma})^3$
Kurtosis	$k = \frac{1}{N}\sum_{j=0}^{N-1}(\frac{x_j - \bar{x}}{\sigma})^4 - 3$

Table 3.3: Different moments of a distribution function

As Fig. 3-16 shows the different type of inboard and outboard fluctuations. The inboard signal shown in thick ink has fewer bursts, while the outboard signal is characterized by the recurring large magnitude bursts.

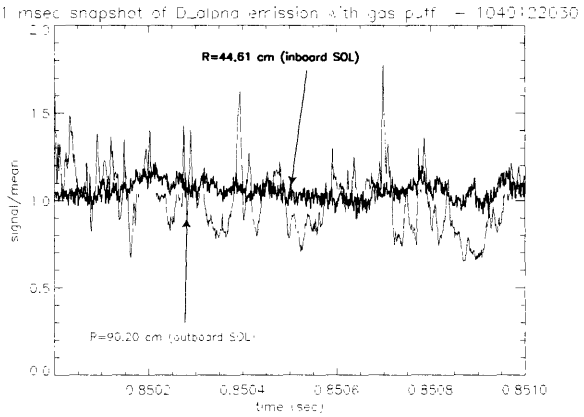

Figure 3-16: Outboard vs. inboard fluctuations

3.6.1 Mean, skewness and kurtosis of the plasma fluctuations

We start by evaluating the different moments of the D_α emission fluctuation time series. In Tab. 3.6.1, we define the first four statistical moments of a distribution function. At different locations the absolute plasma brightness is different, so the quantity $\frac{\sigma}{\bar{x}}$ is plotted versus distance. The standard deviation is normalized by dividing by the mean of the time series at each spatial location.

Skewness is a measure of the asymmetry of a distribution function. The distribution function is symmetric if it is symmetric about the mean. Negative skewness indicates that the distribution has relatively higher number of lower amplitude events,

and positive skewness indicates that the distribution has a larger number of large amplitude events. Kurtosis is a measure of peakedness of the distribution function. The normal distribution has a kurtosis of 3, therefore the kurtosis defined in 3.6.1 is the excess kurtosis. Positive excess kurtosis indicates a distribution with a narrow peak and negative kurtosis shows a flat distribution.

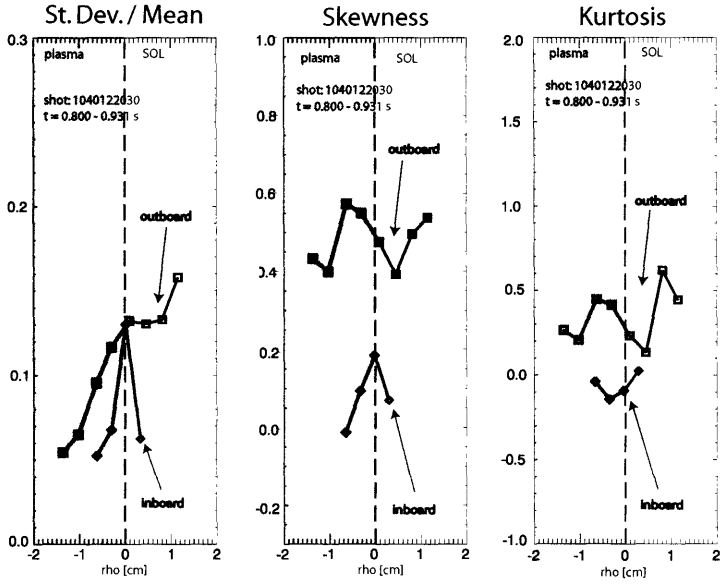

Figure 3-17: The statistical profile of the D_α emission of shot 1040122030 with gas puffing

Fig. 3-17 compares the statistical moments of both inboard and outboard plasma locations. The distance from the separatrix is plotted on the x-axis, indicated by ρ in units of cm. Locations with the same ρ are on the same flux surface. The outboard midplane plasma locations have higher $\frac{\sigma}{\bar{x}}$ ratio than the inboard side. The distribution functions of the outboard views are strongly skewed toward the higher plasma emissivity values. The kurtosis section of the diagram shows that the outboard fluctuation distribution functions are more peaked than the Gaussian and are further away from the normal distribution than the inboard side.

3.7 Radial cross correlations and correlation length

The cross correlation for two separate time series x and y of the same length is defined as

$$C_{xy} = \frac{\sum_{k=0}^{N-1}(x_k - \bar{x})(y_k - \bar{y})}{\sqrt{(\sum_{k=0}^{N-1}(x_k - \bar{x})^2)(\sum_{k=0}^{N-1}(y_k - \bar{y})^2)}}. \tag{3.7}$$

We will now simply calculate the cross correlation for each two neighboring radial views. The typical distance between neighboring views is 4 mm with a diameter of 3.8 mm for each circular view. Since the correlation between two points is not the property of either of the two plasma locations, but the averaged property of the plasma region connecting the two points, we will assign the radial coordinate as the average of the two correlated locations.

Fig. 3-18 depicts the cross correlation profile of shot 1050304012 in the outboard edge plasma during the local neutral gas puff. The cross correlation is defined by Eq. 3.7. Shot 12 from that day is a typical profile and it was chosen because the positioning of the plasma edge was such that there was a view located very close to the position of the separatrix. While all neighboring views have positive correlations, the two views located just outside the separatrix ($\rho_1 = 0.87$ mm, $\rho_2 = 7.4$ mm) have a correlation -0.262. If time averaged cross correlations are taken across the separatrix, the correlation is usually negative.

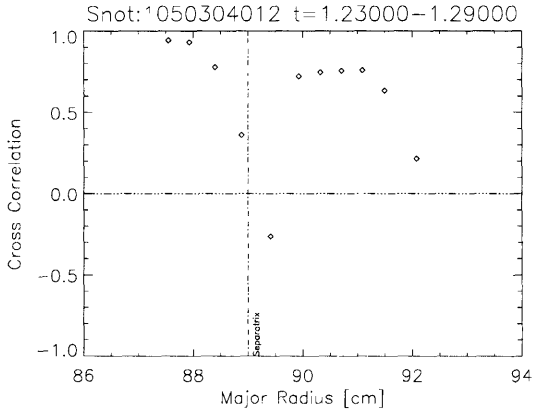

Figure 3-18: Radial cross correlation profile of shot 1050304012

To account for the distance between two neighboring views that are cross correlated, we want to define a local plasma property that has dimensions of length and says something about the correlation.

The correlation length in a medium with spatial extent is usually defined as the width of the spatial auto-correlation curve at each point. This property is ill defined in our case of having 12 or 10 (radial and poloidal, respectively) discrete spatial measurements, because on both sides of the linear viewing arrays, the fluctuation series can not be spatially shifted any further.

Fortunately, this does not present any difficulty when computing the auto-correlation time, as the time series available for time lagged correlation of 130,000 data points is much larger than the usual maximum temporal shift required for the temporal auto-correlation plot (75 data point representing a time shift of 75 μs). The temporal auto-correlation function will be presented in the time lagged correlation section.

One nevertheless is interested in assigning a length-scale to the spatial correlation in the plasma edge region.

We define the correlation length between points A and B separated by a distance d as the distance that would be required for the correlation to drop from one (in the case of $A = B$) to $\frac{1}{e}$ using the rate of spatial correlation decay sampled from the interval $\bar{AB}$.

To test this newly defined quantity, the limits should be now examined. If the steady state cross correlation between A and B is one, then the correlation length is infinity, meaning, then one would have move away infinitely far on the line determined by $\bar{AB}$ for the correlation to drop.

If the cross correlation between A and B is $1/e$, then the correlation length is d, or simply the distance between A and B.

If the cross correlation was zero between A and B, then the correlation length is not defined. For negative values of the correlation, the correlation length is given based on the absolute value of the correlation, in which cases, an additional negative sign of the correlation length indicates the negative cross correlation between points A and B.

For $C_{xy} > 0$,

$$l = -\frac{d}{\ln C_{xy}} \tag{3.8}$$

For $C_{xy} < 0$,

$$l = \frac{d}{\ln |C_{xy}|}. \tag{3.9}$$

Where d is the distance between the neighboring views that are cross correlated.

As Fig. 3-19 shows the radial correlation length ranges from as much as 6 cm (inside the separatrix) to -1cm.

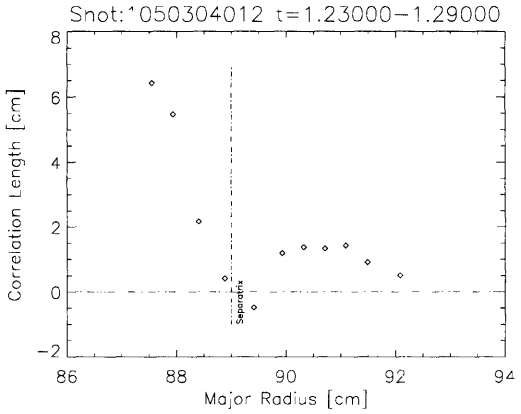

Figure 3-19: Radial correlation length profile of shot 1050304012

3.8 Poloidal cross correlations and correlation length

In a similar fashion to the radial correlation profile we first plot the dimensionless correlation between neighboring views as described by Eq. 3.7.The poloidal correlation profile (Eq. 3-20) does not exhibit negative values as opposed to the radial profile.

In the poloidal direction the poloidal correlation length is also defined as the approximate distance required between two points so that the correlation drops to $\frac{1}{e}$. The poloidal correlation length is varying around 2cm.

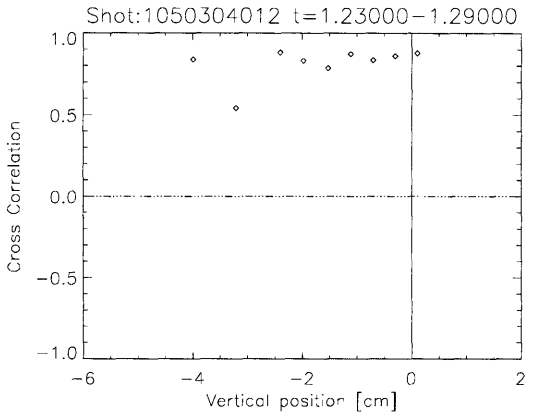

Figure 3-20: Poloidal cross correlation profile of shot 1050304012

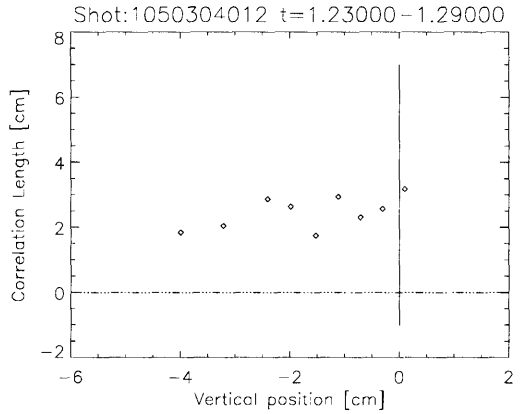

Figure 3-21: Poloidal correlation length profile of shot 1050304012

3.9 Time dependent correlations in the edge plasma

When we look at the different radial channels closely, we notice radially outward propagating local maxima. Fig. 3-22 shows one of these *blobs* as it makes its way away from the plasma toward the wall. There is now a large amount of documentation of this phenomenon. [11][4][1]

As we have looked at the spatial correlation of two points in the plasma edge, we have found that there is a varying level of correlation in radial direction and a high, constant level of correlation in the poloidal direction. In radial direction the plasma edge is divided into two separate regions across the separatrix, while in

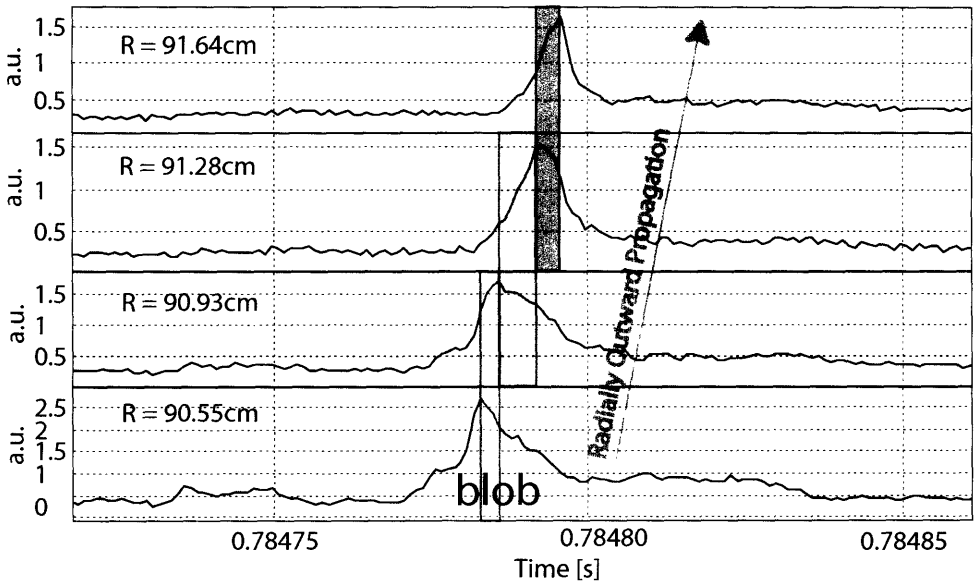

Figure 3-22: Radially outward propagating local maximum. The y-axis has arbitrary units of D_α intensity.(Shot: 1031204007

poloidal direction the steady state correlation between neighboring views is relatively constant. To examine the dynamics of propagating fluctuation we perform a time lagged correlation analysis.

The time lagged correlation between population x and y with a time lag of $L > 0$ is given by

$$C_{xy}(L) = \frac{\sum_{k=0}^{N-L-1}(x_k - \bar{x})(y_{k+L} - \bar{y})}{\sqrt{(\sum_{k=0}^{N-1}(x_k - \bar{x})^2)(\sum_{k=0}^{N-1}(y_k - \bar{y})^2)}} \tag{3.10}$$

and for $L < 0$

$$C_{xy}(L) = \frac{\sum_{k=0}^{N-|L|-1}(x_{k+|L|} - \bar{x})(y_k - \bar{y})}{\sqrt{(\sum_{k=0}^{N-1}(x_k - \bar{x})^2)(\sum_{k=0}^{N-1}(y_k - \bar{y})^2)}}. \tag{3.11}$$

The range of time lag is from -50 μs to +100 μs on Fig. 3-23. The numbers to the right of the figure give the average radial location of the two neighboring views that are being correlated. The maximum correlation has a peaked maximum in most cases. With the exception of the three curves at the bottom, all other locations have well defined maximum correlations. The time lags corresponding to these maximum values

range between -7 and +12 μs. The non-zero well defined lag between points A and B implies a phase velocity in the temporal distribution of D_α brightness fluctuations.

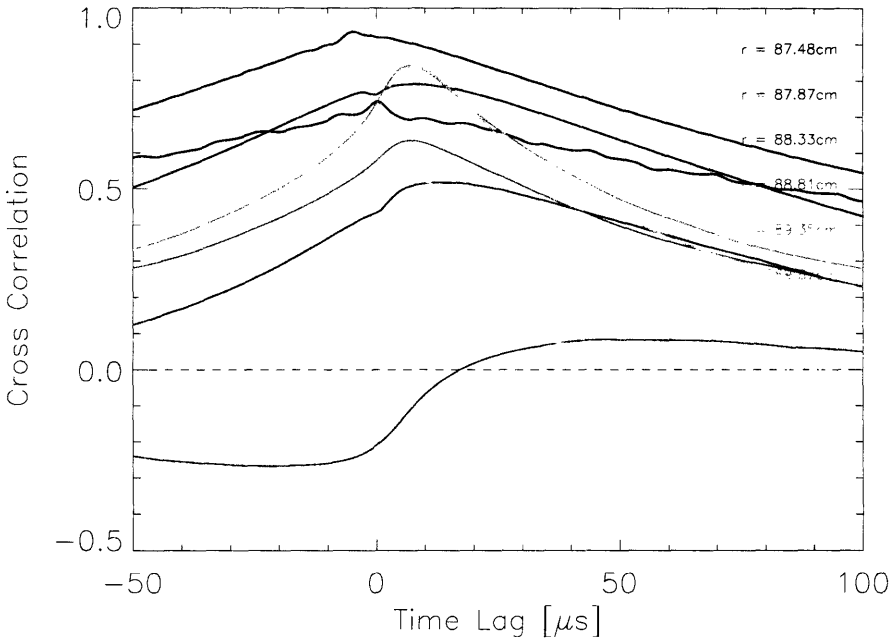

Figure 3-23: Lagged radial correlation profile of shot 1050304012. The correlation is calculated between neighboring views.

Unlike the radial lagged correlation profile, the poloidal lagged correlation profile in Fig. 3-24 does not have negative correlation series. The individual correlation curves are also more alike and follow the same pattern. Each curve corresponds to a vertical position given on the right side of the plot. The line colors get lighter as the vertical position decreases. A larger version of this plot is in the appendix.

3.10 Time lagged correlation with respect to a reference channel

The propagation in both radial and poloidal directions becomes more apparent once the cross correlation is calculated with respect to the same reference channel, rather than between neighboring views.

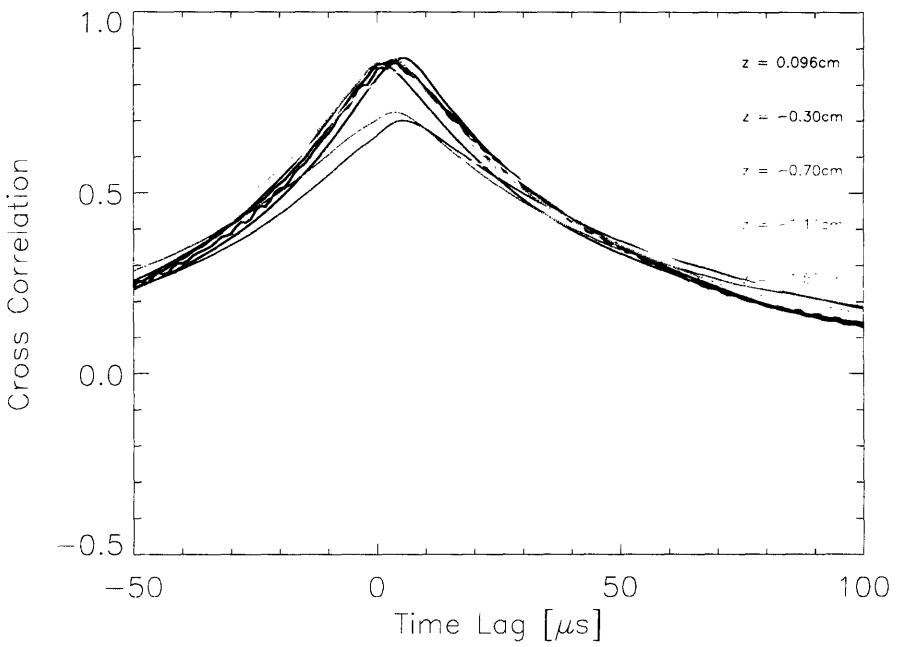

Figure 3-24: Lagged poloidal correlation profile of shot 1050304012. The correlation is calculated between neighboring views.

The most informative plots are generated if the reference channel is chosen around the spatial center of the series. This way in the case of uniform propagation, the correlation curves would peak at both negative and positive lag times.

As already seen, Fig. 3-25 shows both negative and positive correlations on the radial profile.

The poloidal profile as shown in Fig. 3-26 has only positive correlations and as expected for a uniform outward propagation, the locations inside of the reference channel have negative time lags and the locations outside of the reference channel have positive time lags.

On both the radial and the poloidal profile the correlation curve reaching 1.0 is an auto-correlation curve of the reference channel. The width of the auto-correlation curve is related to the life time of the brightness fluctuations. If the auto-correlation time is defined as the full width half maximum of the auto-correlation curve, then the typical auto-correlation time is 60 μs. Both Fig. 3-25 and Fig. 3-26 can be found

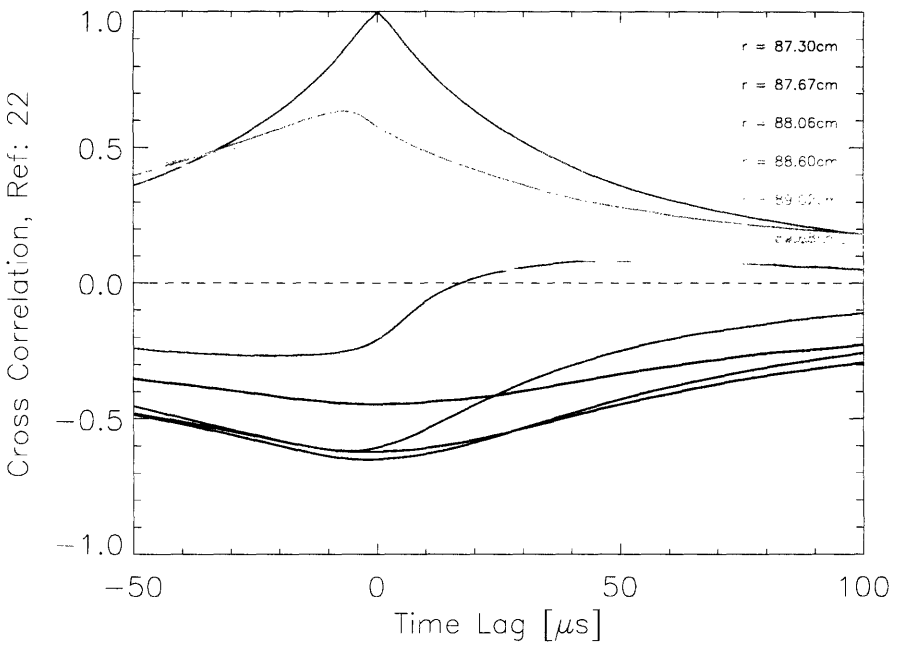

Figure 3-25: Lagged radial correlation profile of shot 1050304012. The correlation is calculated with the reference view of diode 22 with $r = 89.68$ cm.

in the appendix in a larger version.

3.11 Blob propagation phase velocity

From Fig. 3-23 one can locate the time lag ΔT_{lag} at the maximum cross correlation for each spatial location. We define the phase velocity of temporal correlation as,

$$v = \frac{d}{\Delta T_{lag}}. \tag{3.12}$$

In the radial direction (Fig. 3-27), we define outward as positive. In the vertical direction downward is defined positive. For both dimensions the phase velocity is from -1 to 2 km/s. In the radial direction, there is more irregularity inside the separatrix, but outside in the scrape-off layer, the average phase velocity is around 0.5 km/s. The observed negative phase velocity 1 cm inside the separatrix indicates that locally the direction of propagation is inward.

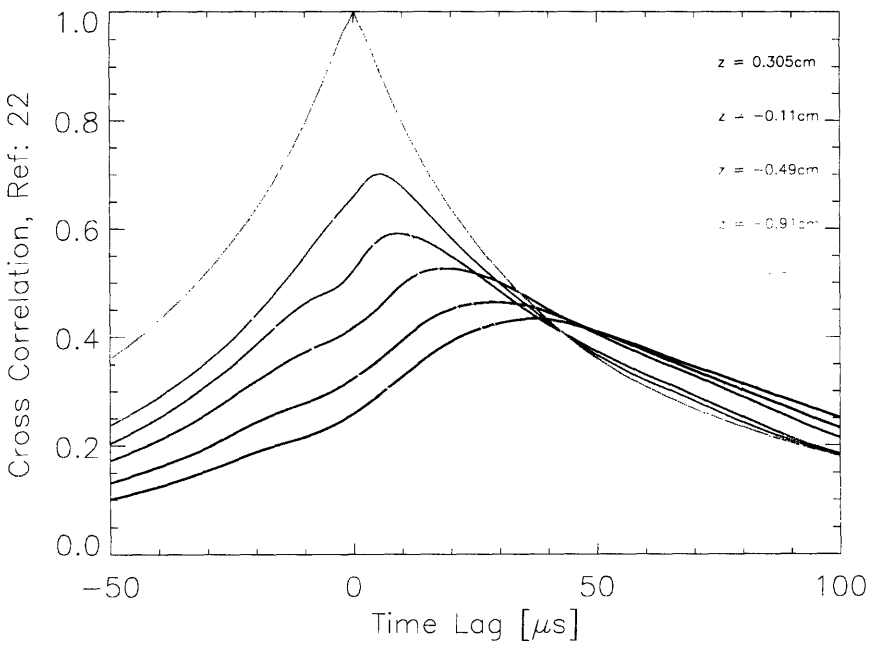

Figure 3-26: Lagged poloidal correlation profile of shot 1050304012. The correlation is calculated between the reference view of diode # 22 with $r = 89.68$ cm and the views with the vertical positions given at the right.

The poloidal phase velocity (Fig. 3-28), is higher and more reproducible on separate shots and time intervals than the radial phase velocity. The poloidal phase velocity is approximately 1 km/s and is pointing vertically downward. This is similar quantitatively with the analysis based on 2-D movies of the D_α emission by Terry et al.[5]

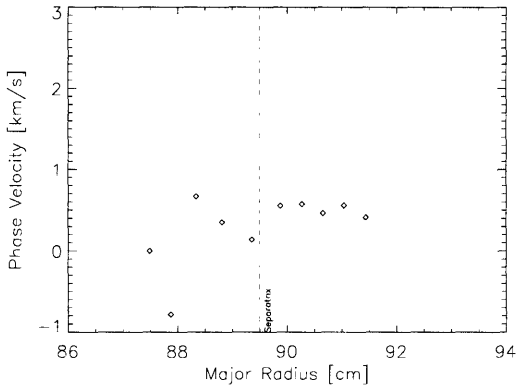

Figure 3-27: Radial phase velocity profile of shot 1050304012

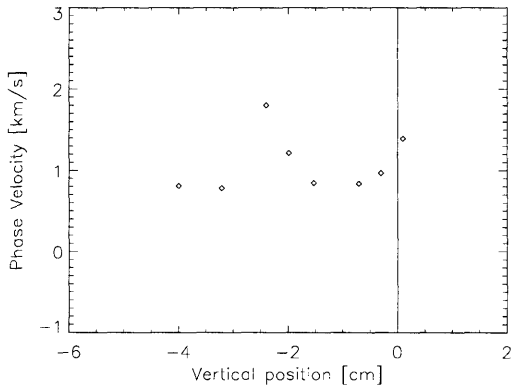

Figure 3-28: Poloidal phase velocity profile of shot 1050304012

Chapter 4

Summary and Conclusion

4.1 Absolute measurement of D_α plasma emission

One of the objectives of this thesis and the fast diodes diagnostics on C-Mod was to measure the absolute brightness profile of D_α in the edge plasma region. To accomplish this goal, 23 fast photodiodes were connected to low-noise amplifier circuits and the assemblies were equipped with D_α filters. The two in-vessel telescopes were designed to transfer the optical emission signals onto fiber arrays. The outboard viewing arrays were both radial and vertical, while the inboard array is made up of only radial views. The data presented in this thesis was recorded by the hardware presented in Chapter 2.

The outboard cross-shaped viewing array enables the reconstruction of the steady-state radial and poloidal profiles of the plasma edge D_α emission fluctuations. To enhance the intensity of the plasma edge D_α emission, a D_2 neutral gas puff is puffed radially locally inward into the edge plasma region. The injected neutral gas increases the brightness up to 20 times and the intrinsic D_α emission toroidally localizes the D_α emission to the gas puffing plane.

The absolute calibration of all 23 photodiode channels, including the transfer fibers, amplifier circuits, filter units and optical apertures allows for the reconstruction of the absolute radial and poloidal profiles of the D_α brightness of the edge region. The largest errors in the absolute measurement arise from the inconsistent reproducibility

of the mechanical optical apertures. The optical apertures need to be varied to prevent saturation of signal from the amplifier circuits.

The plasma discharges analyzed in this thesis can be divided into two large groups. One with the presence of the D_2 neutral gas puff from the specially designed midplane nozzle between the A-B limiters, the other without the gas puff.

The plasma discharges employing the gas puff gave precise measurements of the increase in the D_α brightness due to the gas puff. From the poloidal D_α profile the vertical and, by implication, the toroidal extent of the neutral gas puff is also estimated for the first time.

During shot 1050626002 for example, the peak of the D_α brightness reached $\sim$110 W/m^2/ster, a seven fold increase from the intrinsic D_α brightness of 15 W/m^2/ster. The FWHM vertical extent of the gas puff is estimated at 5 cm.

The intrinsic radial and poloidal D_α brightness and emissivity profiles were measured using the largest aperture openings so as to increase signal level and minimize calibration uncertainties. Once the chord integrated brightness is measured at different discrete locations, the discrete Abel inversion technique is used on a fitted analytical brightness profile to determine the intrinsic D_α radial emissivity profile of the outboard plasma. In this process the diagnostic chords were assumed parallel with the edge plasma being optically thin at the D_α frequency.

The intrinsic radial D_α fitted brightness from shot 1050603013 peaks at 1 cm outside the separatrix at $\sim$11 W/m^2/ster. The plasma edge D_α brightness was assumed to go to zero at $r = 95$ cm and the corresponding Abel inverted D_α emissivity profile peaks at 30 W/m^3/ster. The radial inboard D_α brightness profile was also Abel inverted, and the inboard radial locations were mapped onto the outboard midplane. The outboard and inboard D_α emissivities are found similar. The inboard and outboard measurement of intrinsic D_α brightness are the first to compare *absolute* D_α intensities inboard to outboard.

During shot 1050603013, the fast photodiodes recorded several transitions between the L and H-modes of plasma confinement. The steady state brightness profiles are compared for the L and H-modes, with an added comparison between the inboard

versus outboard plasma edge regions.

4.2 Correlation length and phase velocity

The time lagged correlation of the D_α brightness fluctuations between nearby points in the plasma edge shows evidence of propagating local maxima in the brightness profiles. As can be seen from time lagged correlation calculations, the phase velocity of these propagating structures changes as a function of radial location.

From a direct microscopic point of view, one can identify self-contained local maxima, with typical blob-like shapes in the raw brightness signal. These maxima are seen to be propagating radially outward. Negative blobs or local dark spots can not directly be seen on fluctuation plots, but could also play a role in the observed statistical time-dependent propagation phenomena.

After determining the time lag between each neighboring view, one can measure the phase velocity of the propagating structures. This radial phase velocity is somewhat discontinuous inside the separatrix, ranging from -1 to 2 km/s, but becomes more steady outside the separatrix at approximately 0.5 km/s, where the positive velocity indicates radially outward motion.

The sign changing phase velocity inside the separatrix perhaps suggests that these wave like structures form in the region of high density and temperature gradients. It is not clear however, if this velocity is directly coupled to the local plasma fluid velocity or other drift velocities. Answering this question could bring us a step closer to understanding the energy and particle loss transport mechanisms.

The poloidal phase velocity profiles show vertically downward propagation, with velocities in the range of 1 to 2 km/s. This trend is reproducible from discharge to discharge.

4.3 Comparison with the Xybion camera

Earlier work by S. Zweben, Terry al. [11][12][5], captured an ultra fast framing video of the edge plasma phenomenon also at D_α wavelengths. As shown in Fig. 4-1, the six consecutive frames depict the time evolution of the brightness structures. Areas of increased brightness can be recognized and traced across the subsequent frames. On this example, the blob is propagating radially outward and vertically downward. This is qualitatively similar to the observations of the fast photodiodes as detailed in this thesis.

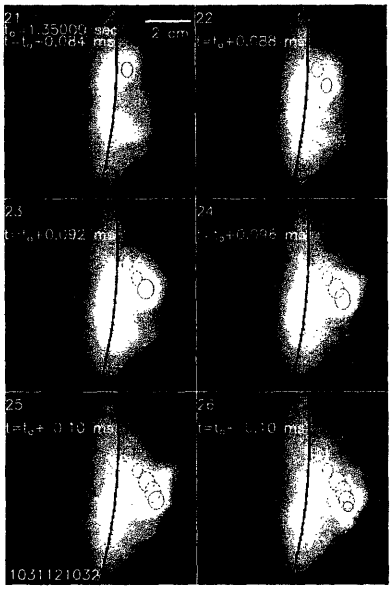

Figure 4-1: Radial and poloidal brightness structure near the separatrix of Alcator C-Mod (Terry at al., 2005)[5]

4.4 Future work

There are many areas recognized for possible future work and exploration. Changing the view of the telescope is a possibility, but a constraint arises from the limited focal length range of the viewing telescope. One may expect similar radial D_α brightness fluctuation profiles at other poloidal angles on the same flux surface, although inboard midplane views have already shown that are much reduced fluctuation levels and no

significant blobs in this region.

A wide angle telescope with variable focal length would be of great value, since the field-of-view and spatial resolution could then be varied over a large range.

From the experimental setup point of view, the design of an electronic aperture control mechanism could help to precisely record the exact position of the optical apertures on each channel. The uncertainty associated with the less than optimal reproducibility on the optical apertures could be overcome by an electronic control system which permanently monitors the exact area of the opening based on a calibrated benchmark light source.

From the data analysis perspective, one could take further advantage of the numerous ($2^{17} = 131072$) data points in the time series, by taking smaller sub intervals on the entire set. These sub intervals could still have statistically satisfying number of elements and could be lined up into a video showing the time evolution of both the absolute brightness profile and the time lagged correlation diagrams.

Lastly, as from the edge transport point of view, one would like to find out how much transport is associated with the observed D_α brightness maxima propagating radially outward and vertically downward.

Appendix A

Figures

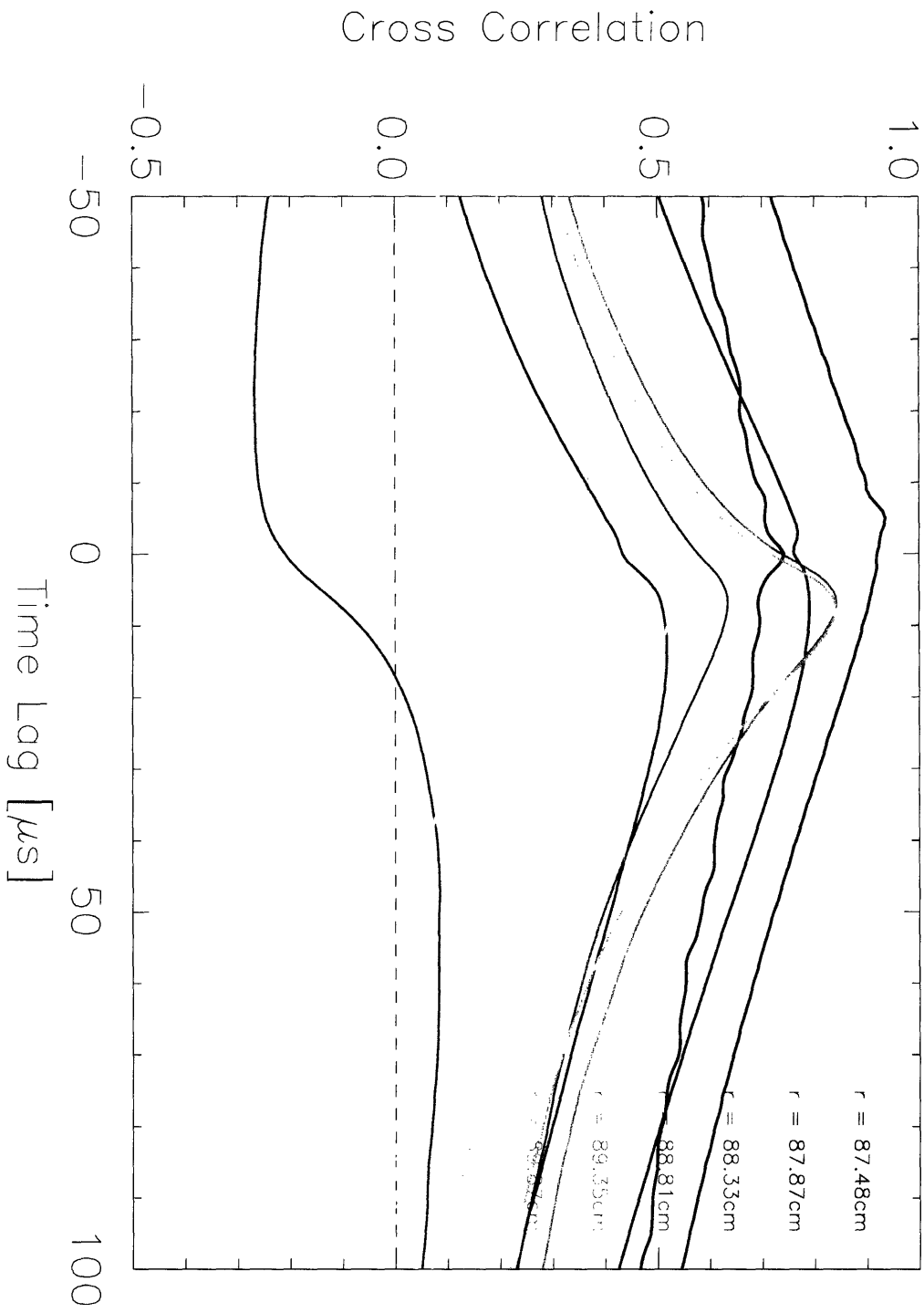

Figure A-1: Lagged radial correlation profile of shot 1050304012.

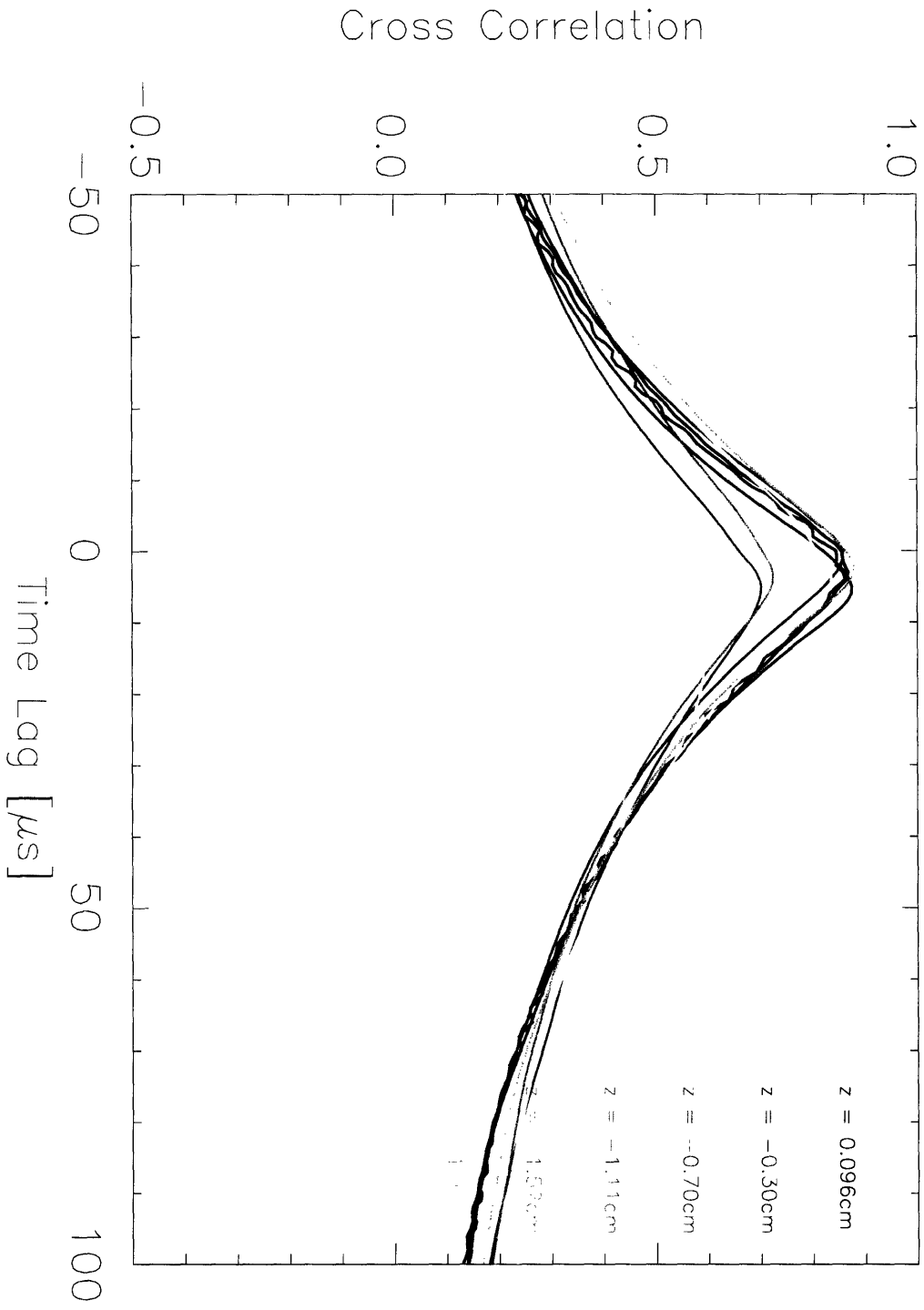

Figure A-2: Lagged poloidal correlation profile of shot 1050304012.

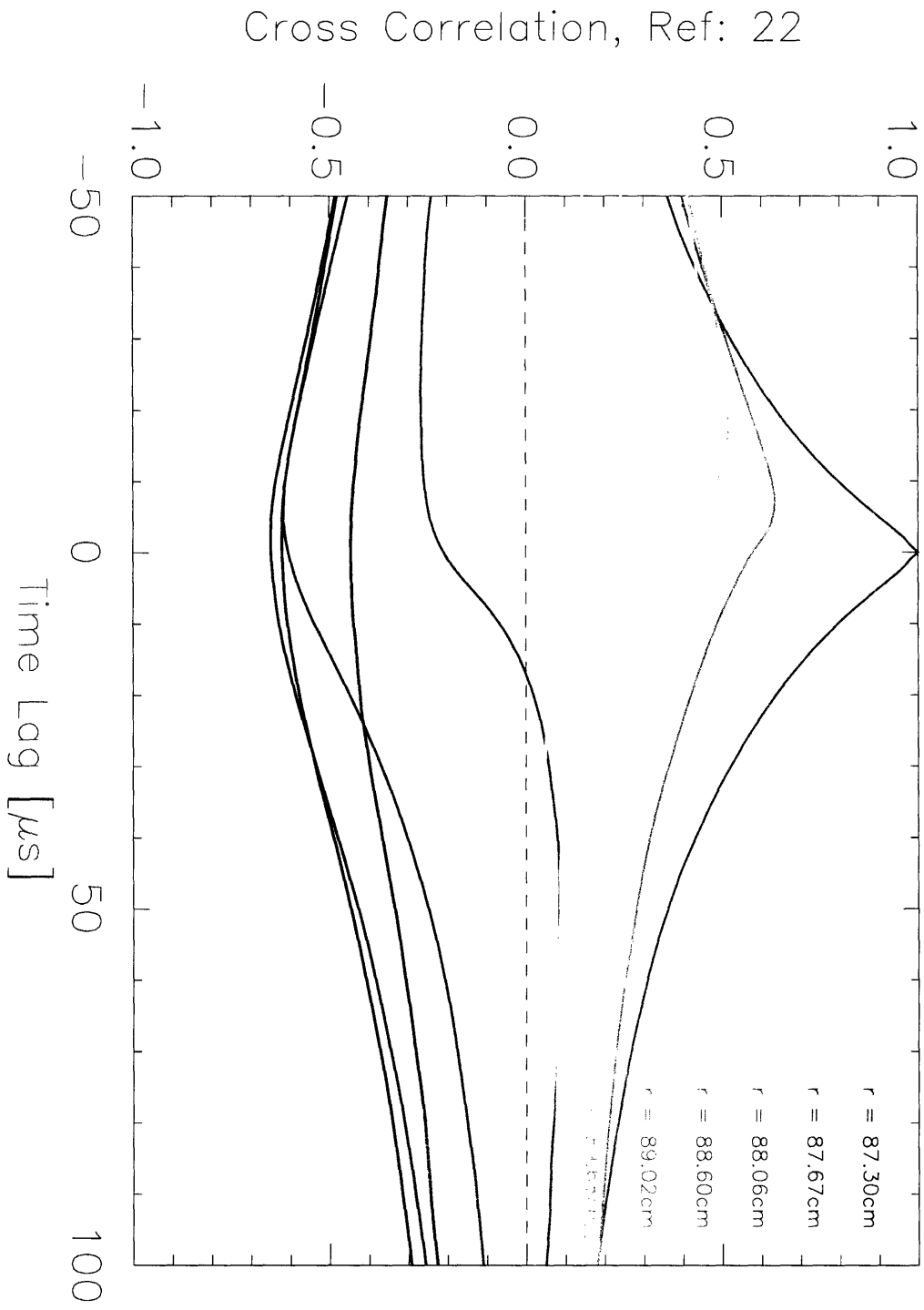

Figure A-3: Lagged poloidal correlation profile of shot 1050304012.

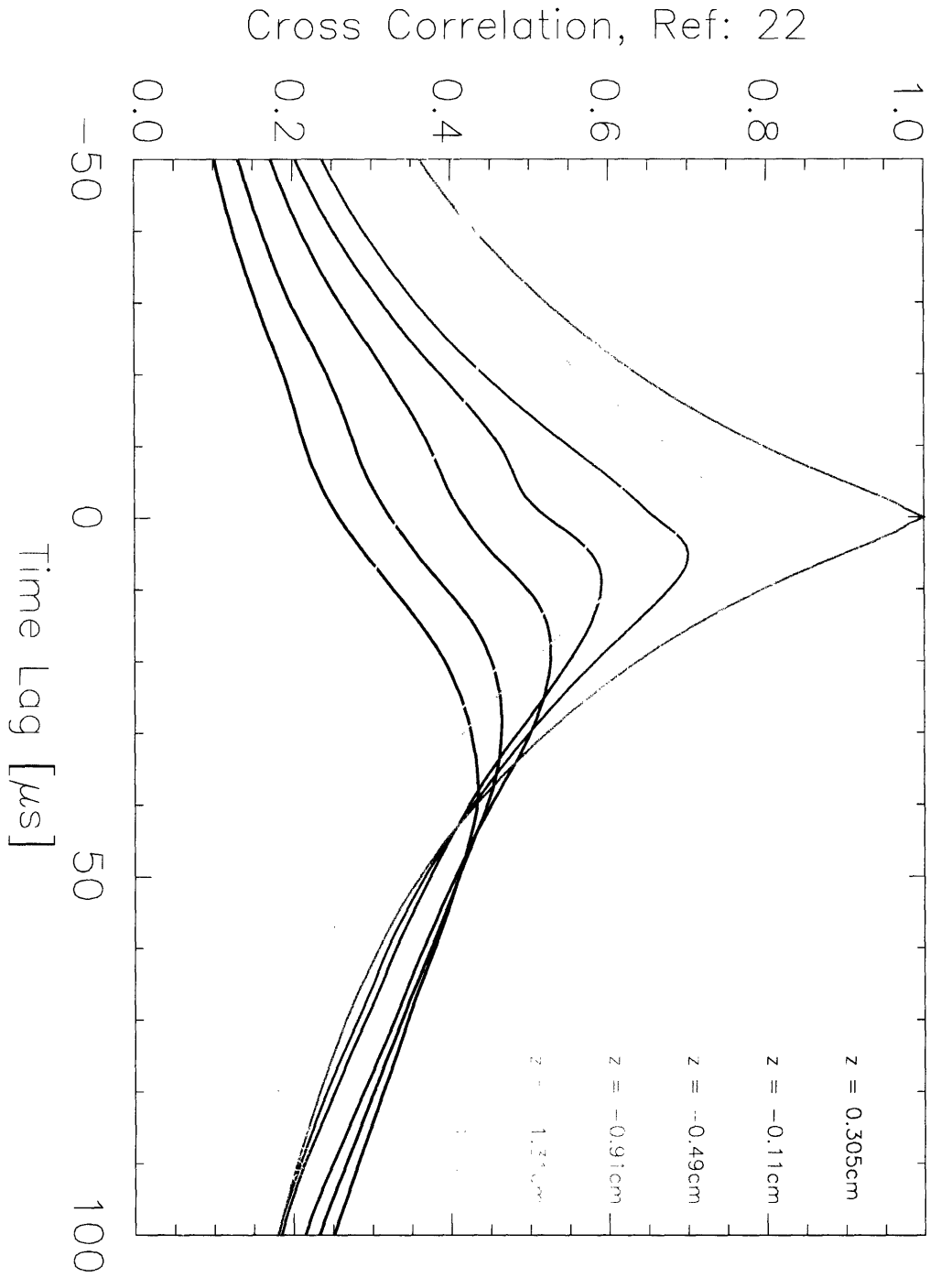

Figure A-4: Lagged poloidal correlation profile of shot 1050304012.

Appendix B

Codes

B.1 Labsphere calibration code

my_labpshere_calibration.pro

```
;Labsphere brightness as follows in mW/cm^2/ster/micron for 728 ft lamberts
; these are the calibrated brightnesses in mW/cm^2/ster/micron for the
; diode measurement of 728 ft lamberts. The actual brightness must be
; scaled by any difference in the diode reading. To put the brightness
; in units of mW/cm^2/ster/nm, multiply these values by 1.e-3.

wavelength=[3200,3400,3600,3800,4000,4200,4400,4600,4800,5000,5200,5360,
5750,6000,6550,7000,7500,8000,9000,10600,11000,12000,13000,15000,17500,
18500.]/10
brightness=[6.80e-3,3.37e-2,9.00e-2,1.83e-1,3.51e-1,5.61e-1,8.32e-1,
1.16,1.54,1.95,2.41,2.79,3.73,4.33,5.55,7.41,7.71,7.71,7.35,7.60,7.43,
6.04,5.52,2.16,1.58,1.14]

;PLOT, wavelength, brightness

;Filter Function
```

```
;this is the supplied filter transmission for Andover D_alpha filter
;SN K122-06 installed in diode #7 which was used for the absolute
;sensitivity calibration of the fast diodes.

filter_wavelength=[646.0,648.0,650.0,651.,652.0,653.,654.0,655.,656.0,
658.0,660.0,661.,662.0,663.,664.0,666.0,668.0,670.0]
filter_transmission=[0.,0.01,0.04,0.07,0.20,0.37,0.62,0.73,0.75,0.74,
0.72,0.63,0.45,0.25,0.1,0.03,0.01,0.]

PLOT, filter_wavelength, filter_transmission, xtitle = 'Wavelength (nm)',
 ytitle = 'Transmission fraction', charsiz = 1.5

;Now interpolate labsphere brightness such that we create values
;corresponding to each filter fuction wavelength.

interpolated_labsphere_brightness = SPLINE(wavelength, brightness,
 filter_wavelength)
;PLOT, filter_wavelength, filter_transmission * interpolated_labsphere_brightness,
 xtitle='Wavelength (nm)', ytitle='Filtered Brightness (microW/cm!u2!N/st/nm)',
 charsiz=1.5

PRINT, 'filtere labsphere brightness integral:',INT_TABULATED(filter_wavelength,
 filter_transmission * interpolated_labsphere_brightness)

PRINT, 'Transmission of the filter at lambda = 656.1 nm:', 0.75
END
```

Bibliography

[1] J. A. Boedo. Transport by intermittent convection in the boundary of the diii-d tokamak. *Phys. of Plasmas*, 8(11), 2001.

[2] A. Mazurenko et al. Experimental and theoretical study of quasicoherent fluctuations in enhanced d_α plasmas in the alcator c-mod tokamak. *Phys. Rev. Let.*, 89(22), 2002.

[3] D. P. Stotler et al. Neutral transport simulations of gas puff imaging experiments on alcator c-mod. *Journal of Nuclear Materials*, 2003.

[4] J. L. Terry et al. Observations of the turbulance in the scrape-off-layer of alcator c-mod and comparisons with simulation. *Phys. of Plasmas*, 10(5), 2003.

[5] J. L. Terry et al. Velocity fields of edge/scrape-ff-layer turbulance in alcator c-mod. *Jounral of Nuclear Materials*, 337, 2005.

[6] M. C. Zarnstorff et al. Circulated presentation. *Phys. of Plasmas*, 4, 1993.

[7] M. Endler et al. Measurments and modelling of electrostatic fluctuations in the scrape-off layer of asdex. *Nuclear Fusion*, 35(11), 1995.

[8] M. Greenwald et al. Characterization of enhanced d_α high-confinement modes in alcator c-mod. *Phys. of Plasmas*, 6(5), 1999.

[9] Mark A. Meier et al. Adiabatic electron thermal pressure fluctuations in tokamak plasmas. *Phys. Rev. Let.*, 87(8), 2001.

[10] R. J. Fonck et al. Low noise photodiode detector for optical fluctuation diagnostics. *Rev. Sci. Instrum.*, 63(10), 1992.

[11] S. J. Zweben et al. Edge turbulence imaging in the alcator c-mod tokamak. *Phys. Plasmas*, 9(5):1981–1989, 2002.

[12] S. J.Zweben et al. High speed imaging of edge turbulence in nstx. *Nuclear Fusion*, 44(134), 2004.

[13] G. W. Forbes. *J.Opt.Soc.Am.*, 5, 1988.

[14] I. H. Hutchinson. *Principles of Plasma Diagnostics*, chapter 4. Cambridge University Press, 2 edition, 2002.

[15] J. D. Lawson. Some criteria for a power producing thermonuclear reactor. *Proceedings of the Physical Society*, 70(6), 1957.

[16] J. R. Myra. Plasma convection by blobs in the scrape-off-layer. *31st EPS, London, June 28 - July 2*, 2004.

[17] Beer H. Palme H. *Abundances of the elements in the solar system*, volume 3 of *Astronomy and Astrophysics: Instruments; Methods; Solar System*, pages 196–221. Springer, Berlin, 1993.

[18] P. C. Stangeby. *The plasma boundary of magnetic fusion devices.* IOP Publishing Ltd., 2000.

[19] M. V. Umansky. Comments on particle and energy balance in the edge plasma of alcator c-mod. *Phys. of Plasmas*, 5(9), 1998.